Lifting the degeneracy of optical fiber neural interfaces for optogenetics and electrophysiology by using axialtrodes

Authors: Kunyang Sui[1,3], Neela K. Codadu[2]*, Daman Rathore[2]*, Guanghui Li[3], Marcello Meneghetti[1,3], Rune W Berg[3], Rob C. Wykes[2,4] and Christos Markos[1,5]

Affiliations:

[1]DTU Electro, Department of Electrical and Photonics Engineering, Technical University of Denmark, Kgs. Lyngby, 2800, Denmark.

[2]Department of Clinical and Experimental Epilepsy, Queen Square Institute of Neurology, University College London, London, WC1N 3BG, UK.

[3]Department of Neuroscience, Faculty of Health and Medical Sciences, University of Copenhagen, Copenhagen, 2200, Denmark.

[4]Centre for Nanotechnology in Medicine & Division of Neuroscience, Faculty of Biology Medicine & Health, University of Manchester, Manchester, UK

[5]NORBLIS ApS, Virumgade 35D, 2830 Virum, Denmark

* These authors contributed equally to this work.

Abstract:
Optogenetics and electrophysiology are powerful methods in neuroscience for precise spatiotemporal control and recording of neural activity. Conventional flat optical fibers, commonly used in deep brain regions, can only interface with limited tissue volume at their distal end. However, depth-resolved neuromodulation and recordings are crucial for decoding neuronal connections across various brain domains. In this work, we address this limitation by introducing an axialtrode developed using soft polymers integrated with multiple metal electrodes via a scalable thermal drawing process. We employ the developed fiber-based neural interface, controllably angled-cleaved, for multisite optogenetics and electrophysiology at different brain regions. Its suppressed inflammatory responses indicate improved biocompatibility compared to conventional fibers. This concept can be adapted to any fiber material and application where depth-resolved stimulation and electrical recordings are important, bringing the community a step closer to understanding complex neuronal dynamics.

INTRODUCTION

The exploration of neural dynamics in the brain is pivotal for elucidating the mechanisms by which neurons encode information and subsequently influence behaviors through inherent connectivity and reciprocal interactions (*1*). To investigate the correlation between the actions of these brain cells and resultant behaviors, it becomes essential to artificially activate or inhibit the cells, concurrently mapping the activity in the surrounding circuitry and documenting changes in behavior (*2*). Despite the high temporal resolution offered by the electric stimulation of neurons, its broad impact on regions near the electrodes within the brain tissue increases the difficulties of cell-type-specific neuronal activity modulation (*3*). Moreover, electrical neuromodulation signals may give rise to "cross-talk" between the stimulating and recording electric signals, thereby introducing major artifacts (*4*).

Interdisciplinary studies offer researchers novel approaches to overcome existing limitations. Optogenetics, a well-established technology that amalgamates genetic and optical methods, stands out by facilitating fast and precise control over specific neural populations and reversible manipulation of neural activities (2). The optical control of neural activities has led to the development of light delivery tools, commonly based on the integration of standard or tapered silica optical fibers with electrodes, to enable the concurrent application of optogenetic control and electrophysiological recording (*5–9*). Leveraging advancements in integrated circuit fabrication and micro-fabrication technology, light sources can also be seamlessly incorporated into traditionally used silicon probes to form monolithic implants (*10–12*).

During the last ten years, polymer-based multimaterial optical fibers have emerged as a versatile platform for developing multifunctional brain implants (*4*, *13–17*). Their superior flexibility results in minimal inflammatory responses compared to their silica counterparts (*18*), attracting an increasing number of researchers to this field. Since the first *in vivo* demonstration of their functionality for simultaneous optical, electrical, and chemical interrogation of brain neural circuits in 2015 (*19*), several notable contributions have been made. Park et al. proposed hydrogel hybrid fiber probes to reduce tissue damage induced by brain micromotion post-implantation. These hybrid devices exhibit variable bending stiffness regulated by the hydration states of the hydrogel matrix (*20*). Another noteworthy advancement involves integrating ferromagnetic composites onto multifunctional fibers, resulting in the proposal of a submillimeter-diameter fiber robot for navigable implantation and sensing of electrophysiological signals (*13*). More recently, to leverage infrared neurostimulation (INS) as a transgene-free alternative to optogenetics, Meneghetti et al. developed a bidirectional soft fiber-based device for deep brain INS and simultaneous electrophysiological signal recording (*21*, *22*), using polymer materials capable of transmitting light in the 2 μm wavelength region.

All the reported fiber-based neural implants so far rely on structures that are located at the distal end of the fiber. Thus, akin to spectral lines corresponding to degenerate energy levels, different brain layers in the proximity of the implantation site are indistinguishable in terms of interaction with the implant. However, in brain structures such as the medial prefrontal cortex, where cellular populations are distributed along the dorso-ventral direction (aligned vertically to the brain surface), lifting this degeneracy is crucial for collecting discretized information from distinct neuronal circuits, a task in which conventional flat-end optical fibers fall short (*23*). Furthermore, depth-resolved recordings of the neural activity becomes imperative when the relevant neural circuits span a considerable depth range within the brain as, for instance, when investigating seizures across cortical and hippocampal regions (*24*). Although the issue can be addressed by either positioning a flat-end facet optical fiber above electrode arrays or employing a tapered optical fiber beside electrode arrays (*25*), the integration of a neural interface that combines optical waveguides and electrodes is indispensable to mitigate relative positional uncertainties between sites of optical neuromodulation and neural activity recording at varying depths within the brain.

In this work, we propose a novel way to lift the degeneracy of conventional optical fiber-based neural interfaces by introducing the axialtrode, a device capable of providing light stimulations and neural activity recordings across different brain depths. The axialtrode was developed using a scalable thermal drawing process, integrating various functional materials and scaling them down to the desired dimensions for concurrent optical stimulation and depth-resolved neural activity recording. We used transparent thermoplastics, polycarbonate (PC), and polymethyl-methacrylate (PMMA) as the core and cladding materials, respectively, to form a step-index structure. Eight tungsten (W) microwires were integrated into the cladding of the fiber-based neural device for

high-quality electrophysiology. The angle-cleaved structural geometry of the implant allows the electrodes to be distributed along the fiber axis, enabling electrical signal recording across different depths. This ability has been investigated by spatially distinguishing the intensity of theta rhythm between cortical and hippocampal regions in rodent models. *In vivo* experiments demonstrated the reliable performance of the axialtrode through simultaneous optical stimulation and electric signal recording, while importantly, they offered a reduced inflammatory response compared to their flat counterparts. .

RESULTS

Design and fabrication of polymer optical fibers

The concept of our proposed axialtrode design, featuring an integrated optical waveguide and eight spatially distributed electrodes, is illustrated in **Fig. 1A**. This multifunctional device is based on a step-index polymer optical fiber fabricated using a thermal drawing process. Specifically, PC and PMMA were chosen as the core and cladding materials due to their thermo-mechanical compatibility, overlapping viscosity-temperature profiles (*26*) and distinct refractive indices (*27*). During thermal drawing, a macroscopic preform, prepared by rod-in-tube method as depicted in **Fig. 1B,** was heated and drawn into a fiber with equivalent cross-sectional geometry but micro-scale dimensions (more details in **Materials and Methods**). It is worth noting that the eight blind bores (hollow channels) with a diameter of 4 mm were added from the lower face of the PMMA tube. These blind bores can help to build up a constant pressure in the hollow channels to maintain the microstructure of the fibers during the thermal drawing process (**Fig. 1C**). In this study, the target fiber diameter ranged between 420 and 440 µm for compatibility with commercially available ceramic ferrules (CFLC440-10, Thorlabs). Several hundreds of meters of flexible polymer optical fiber were successfully produced in a single drawing (**fig. S1**). The cross-section of the drawn PC/PMMA fibers with a core diameter of 200 µm and micro-channels (MCs) diameter of 50 µm is depicted in **Fig. 1D**, illustrating that the eight MCs are distributed equidistantly around the fiber core in the cladding. The fabricated optical fibers can deliver visible light including blue light (470 nm wavelength) and red (650 nm wavelength) for activating commonly used opsins in optogenetics, such as channelrhodopsin-2 (ChR2) and red-shifted rhodopsins, respectively (*28–30*) (**Fig. 1D**).

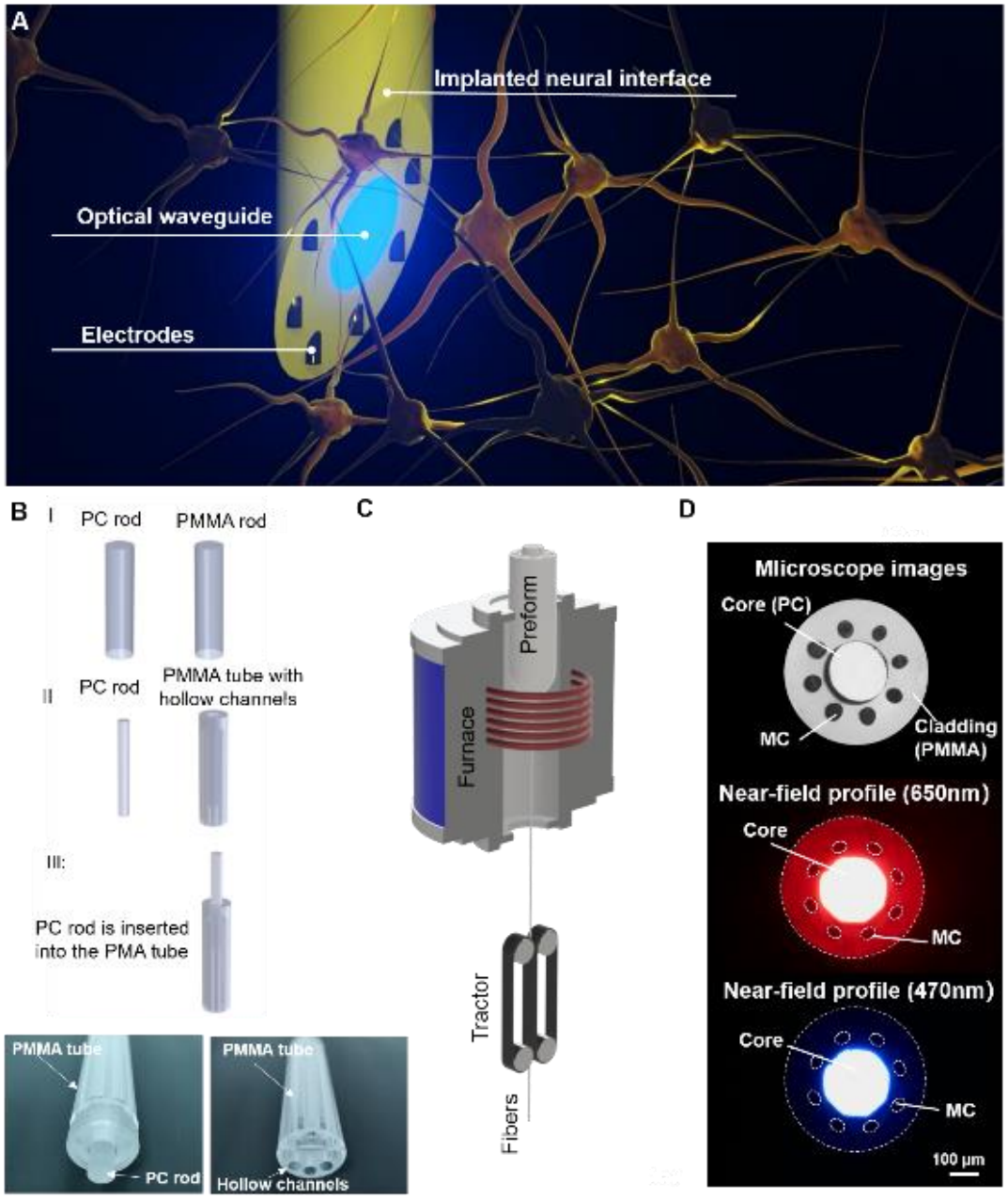

Fig. 1. Concept and development steps of axialtrodes enabled by polymer optical fiber technology. (A) Schematic of the axialtrode with integrated optical waveguide and eight electrodes for neuromodulation and electrical recording of the neural activity. **(B)** The fabrication of the preforms. I: PC rod and PMMA rod were employed as the raw materials. II: The diameter of the PC rod was machined to 10 mm and a central hole with a diameter of 10.3 mm was introduced at the upper surface of the PMMA rod for match with the PC rod. In addition, eight holes with a diameter of 4 mm were added at the lower surface of the PMMA rod. III: The PC rod was inserted into the central hole at the upper surface of the PMMA rod. The lowest images illustrate the details at two ends of the assembled preform. **(C)** Schematic of the thermal drawing process for the production of the PC/PMMA polymer optical fibers. Several tens of meters of fiber can be obtained within a one-time fabrication. **(D)** The cross-section of the drawn PC/PMMA fibers with eight MCs under a microscope (top), the near-field profile of the output light from the PC/PMMA fibers when red light at the wavelength of 650 nm (middle) and blue light at the wavelength of 470 nm (bottom) were delivered by the PC core of the fibers.

Development and characterization of the axialtrode

To enable depth-resolved neural activity recording, it is essential to distribute the electrodes at distinct positions along the axial direction of the optical fiber. This can be realized by introducing an angled-end facet to the fiber. Exploiting the soft nature of polymer materials, we developed a controllable and accurate mechanical cutting/cleaving method for introducing the angled tip based on a customized stainless steel mold (**fig. S2**). The mold features "V" grooves machined onto one surface of a stainless steel block, with the angle between the grooves and the block's edge customized according to the desired angle. During the cleaving process, the fiber was placed in one of the grooves with its tip extending out. Pressure was applied to the upper face of the mold to enhance friction between the fiber and the mold, preventing any unintended movement during cutting. Ultimately, the fiber tip was cleaved by sliding a blade along the side face of the stainless steel block. Angled structures at 90° (flat-cleave), 45°, 30°, and 15°, were produced based on this method as depicted in **Fig. 2A**.

To integrate electrodes into the optical fibers, as depicted in **Fig. 2B**, the MCs within the cladding of the angled-tip polymer optical fiber were exposed using a scalpel from the side surface of the fiber. Tungsten metal wires with a diameter of 50 µm were then integrated into the MCs from the exposed site under a microscope until they appear at the angled surface of the fiber. Subsequently, the position of the tungsten wire was fixed with a small drop of cyanoacrylate adhesive. Ceramic ferrules were attached to one end of the polymer optical fibers to facilitate the connection with commercial silica patch cables (M61L01, Thorlabs) during optical neuromodulation applications. Since the proposed axialtrode incorporates eight tungsten wires functioning as spatially distributed electrodes, a scaffold was created using a 3D printer (Sonic Mighty 8K, Phrozen) to prevent mutual entanglement of the metal wires or any potential unwanted cross-talking (refer to **Materials and Methods** for details on the scaffold development). All eight tungsten wires were connected with a 1.27 mm pin header through the interference fit between pin holders in the scaffold (**fig. S3**). The details of the assembled axialtrodes are presented in **Fig. 2C**. The modest weight (0.6 g) of the assembled axialtrode makes it easy to be securely fixed on the head of mice for *in vivo* experiments (**Movie S1** and **fig. S4**).

Illumination maps at the output end of the angled fiber were simulated using the ray-tracing software Zemax OpticStudio and experimentally verified in a brain slice. In the simulations, we compared the illumination maps of angled-tip fibers (45° and 30°) with that of a flat-end optical fiber (90°) (refer to **Materials and Methods** and **fig. S5** for simulation details). The corresponding results are depicted in **Fig. 2D**. It can be seen that the medium adjacent to the end facet of the axialtrode was efficiently illuminated at different angles. Interestingly, with a reduction in the cleaving angle, part of the light propagates in the core of the fiber and is reflected by the interface between the core and the brain medium (forming *cluster b*) and further reflected by the interface between the cladding and the brain medium (forming *cluster c*) as illustrated in **fig. S6**. In addition, the decrease of the cleaving angle results in a reduced divergence of the emitted light (a smaller angle between the three clusters). **Figure 2E** compares the illumination map differences between fibers with flat end facets, 45°, and 30° angles investigated in real brain slices. It is evident that for the fiber with a 45° angled tip, part of the tissue on the back side of the end facet is illuminated due to reflection by the core-tissue interface, corresponding to the ray *cluster b* in the simulation (as shown in **fig. S6**). When the angle of the axialtrodes is reduced to 30°, more polymer volume must be inserted into the brain tissue for mapping the illumination profile due to the enlarged angled tip length. Despite the strongly compressed tissue around the fiber resulting in serious inhomogeneous tissue density and deformation of the illumination map, it is still evident that tissue

near the tip of the fiber and on the back of the angled end facet has a high illumination intensity (**fig. S7A** and **B**). To minimize tissue deformation during the experimental investigation of the illumination map, the orientation of the brain slice was rotated to maintain the upper surface of the slice in contact with the angled end facet of the fiber. The illumination pattern of the tissue near the end facet of the fiber can be seen in **Fig. 2E**.

The optical characterization of the neural interfaces was assessed by measuring the optical attenuation spectrum of the optical waveguide using the cut-back method (*31–33*). The electrical characterization of the neural interfaces involved measuring impedance spectroscopy with a chemical impedance analyzer (IM3590, Hioki). The loss spectrum of the PC/PMMA polymer optical fibers in the wavelength range of 450 nm to 1100 nm measured using a supercontinuum laser is depicted in **Fig. 2F**. The minimum loss was observed to be approximately 0.1 dB/cm between 750 nm and 850 nm, consistent with prior reports on PC-based polymer optical fibers (*33*). High-loss bands are present between 600 nm and 1100 nm due to the high harmonics of carbon-hydrogen bonds vibration absorption (*34*). The elevated loss region at wavelengths shorter than 600 nm is attributed to the scattering and electronic transition related to ultraviolet absorption (*35*). Despite the pronounced loss in the blue region of the spectrum (470 nm), optical neuromodulation can still be achieved since only a short length of fiber is needed for implantation (*16*, *17*, *20*, *33*). **Figure 2G** displays the measured impedance of the eight electrodes as a function of frequency from 1 Hz to 10 kHz (more detailed characterization results of the impedance and phase of the eight integrated electrodes can be seen in **fig. S8**). Considering electrodes with impedances less than 1 MΩ at 1 kHz region are considered to be suitable for electrophysiology (*36*), the integrated tungsten electrodes are anticipated to provide high-quality signal recordings as we show in the subsequent *in vivo* experiments.

The biocompatibility of the axialtrodes was investigated through immunohistochemical (IHC) evaluation of the recruitment of microglia at the implantation sites. The inflammatory response differences between the axialtrode with a 15° angle tip and the conventional flat end-facet fiber with the same materials and diameter have been experimentally investigated. Here we chose the axialtrode with a tip angle of 15° since the long distance between its topmost and lowest electrodes can be as large as 900 ± 10μm, which is preferable for resolving the depth brain neural activity dynamics and recording in the following *in vivo* experiments. Mice with axialtrodes (N = 2) and standard end-facet fiber (N = 2) implanted were transcardially perfused 4 weeks after the implantation. The ones without any implantation surgeries served as control samples (N = 2). After the brains were dissected and sliced using a cryostat, the slices were stained with marker ionized calcium-binding adaptor molecule 1 (Iba1) and 4′,6-diamidino-2-phenylindole (DAPI) for activated microglial and their nuclei detection, respectively (**Fig. 2H**). The intensity of fluorescence observed within specified regions of interest (ROI) (500 μm x 500 μm) centered at the tip of the inserted fiber was used as an indicator of the reactive microglia induced in the brain by the neural devices. Quantitative analysis across different brain slices indicates a variance in the mean fluorescence intensity levels among the three distinct groups of samples (**Fig. 2I**), with the axialtrode proposed in this work producing less inflammatory response aggression compared with its flat end-facet counterpart ($p = 0.0547$, **fig. S9**). This can be attributed to the reduced foreign body response introduced by the smaller volume of the angled end-facet of the implant combined with the fact that the sharpened axialtrode's tip reduces the tissue compression beneath the device during the implantation process compared with the fiber with a flat end-facet.

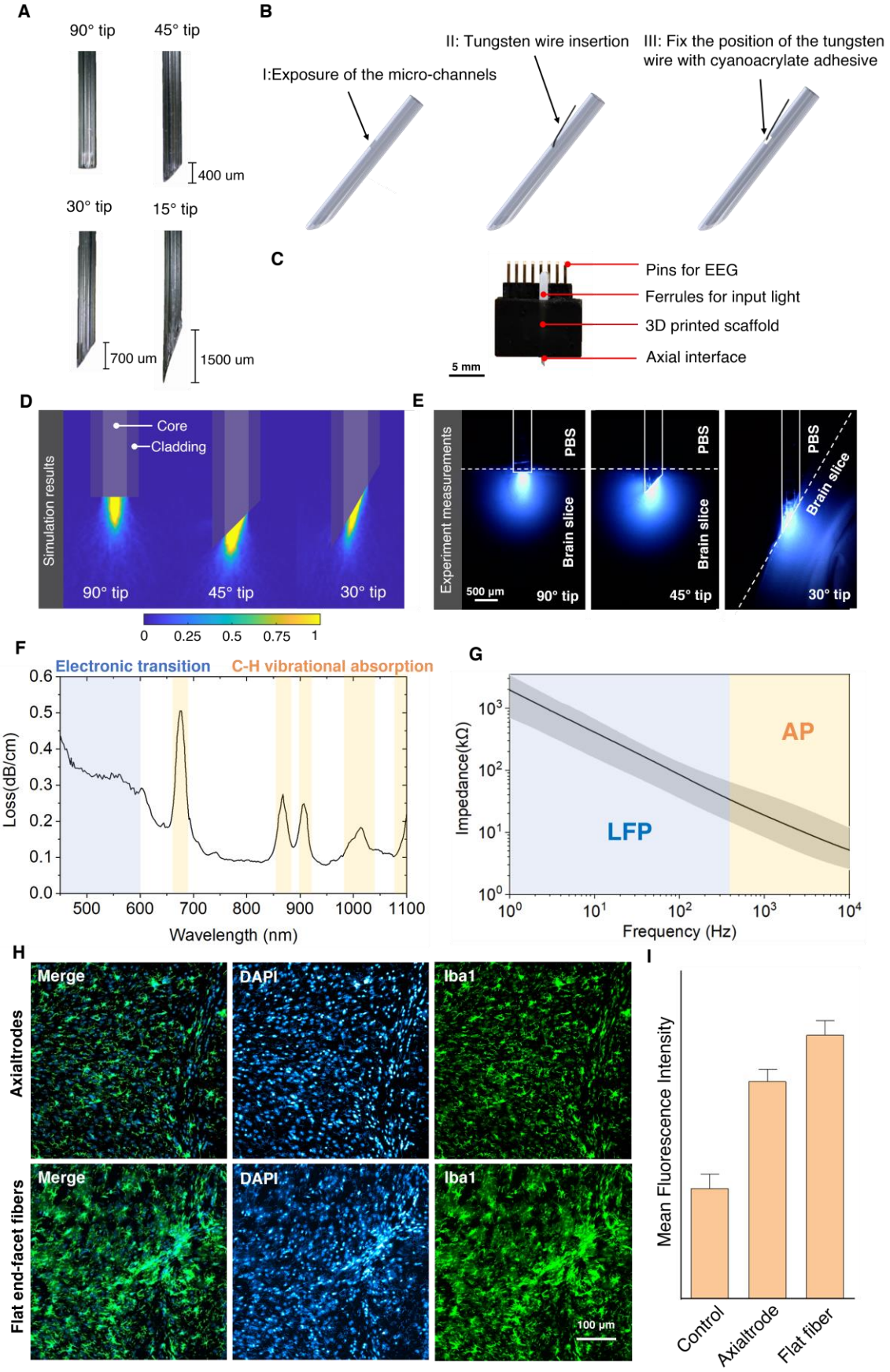
A
90° tip
45° tip
400 um
30° tip
15° tip
700 um
1500 um
B
I:Exposure of the micro-channels
II: Tungsten wire insertion
III: Fix the position of the tungsten wire with cyanoacrylate adhesive
C
Pins for EEG
Ferrules for input light
3D printed scaffold
Axial interface
5 mm
D
Simulation results
Core
Cladding
90° tip
45° tip
30° tip
0
0.25
0.5
0.75
1
E
Experiment measurements
PBS
Brain slice
500 µm
90° tip
45° tip
30° tip
F
Electronic transition
C-H vibrational absorption
Loss(dB/cm)
Wavelength (nm)
G
Impedance(kΩ)
Frequency (Hz)
AP
LFP
H
Axialtrodes
Flat end-facet fibers
Merge
DAPI
Iba1
100 µm
I
Mean Fluorescence Intensity
Control
Axialtrode
Flat fiber

Fig. 2. Development and characterization of the axialtrode. (A) An illustration of different cleaving angles is introduced at the tip of the polymer optical fibers. Here we show the optical microscopy images of fibers with end-facet angles of 90°, 45°, 30°, and 15°. **(B)** Electrode integration process inside the microstructured polymer optical fibers. I: The MCs were exposed from the side of the fiber with a scalpel. II: Tungsten wires with a diameter of 50 µm were inserted into the MCs in the fiber cladding from the exposed side outlets. III: A small drop of cyanoacrylate adhesive was applied to fix the position of the tungsten wires. **(C)** Optical image of the assembled axialtrode in the scaffold. The 3D-printed scaffold was used for the integration of the axialtrode with a ferrule and pin header. **(D)** Simulation results to compare the illumination maps difference between the fibers with tip angles of 90°, 45°, and 30°. **(E)** Measured illumination maps of fibers with tip angles of 90°, 45°, and 30° in fixed brain slices. **(F)** Attenuation profiles of the PC/PMMA polymer optical fibers,measured using cut-back method. **(G)** Measurement of the impedance spectrum of the integrated tungsten wires in the axialtrode as a function of frequency. The results are based on eight measurements on each of the integrated tungsten electrodes. The black line represents the mean impedance value of the eight electrodes, while the grey shading area indicates the range of variation. **(H)** Immunohistochemistry staining of the microglia (Iba1, green) and nuclei (DAPI, blue) 4 weeks after the implantation of the axialtrodes and conventional flat-end facet polymer fibers. **(I)** Mean fluorescence intensity of Iba1 marker in the 500 × 500 µm region centered at the tip of the axialtrodes, conventional flat end-facet fibers, compared with control animals (N slices =7 for each type, 4 weeks implantation). The whiskers of the bar plot represent the standard error.

In-vitro photoelectric artifacts evaluation

During electrophysiological neural activity recording, photoelectric artifacts represent a primary noise factor leading to data contamination and distortion, which was first detailed by French physicist Alexandre-Edmond Becquerel in 1839 (*37*). For metallic materials, the valence and conduction bands typically overlap, making it easy for electrons to be excited by photon energy during light stimulation and result in photoelectric artifacts (*10*, *38*). In addition, the photoelectric artifacts can also be affected by the distance between the optical waveguide and the electrodes (*39*). Consequently, it is imperative to investigate the photoelectric artifacts of the proposed axialtrodes to ensure reliable signal recording.

With the assistance of the 3D printed scaffold and a custom-made pin adaptor, the proposed axialtrodes can be seamlessly connected with commercially available light sources and electrophysiology recording systems for all *in vitro* and *in vivo* experiments (**fig. S10**). *In vitro* measurements of optical stimulation-induced photoelectric artifacts were conducted by coupling a pulsed LED source (470 nm, 10 ms, 10 Hz) to the axialtrode with a 15° tip in phosphate-buffered saline. The experimental setup is schematically illustrated in **Fig. 3A,** while **Fig. 3B** illustrates the temporal relationship between the stimulating light pulse and the resulting artifacts. The photoelectric signals are observed to be triggered at the rising edge of the laser pulse and begin to decrease at the falling edge. Recorded electrical signals from all eight electrodes during blue light stimulation in broadband (1-9000 Hz), the local field potential region (0.1-100 Hz), and the multi-unit activity region (500-9000 Hz) are presented in **Fig. 3C** (the full recordings are illustrated in **fig. S11**). Signals from the upper three electrodes are highlighted with a blue shadow, while signals from the lower three electrodes are marked with a red shadow. It is clear that the lower three electrodes at the angled end facet of the axialtrode experience light-induced electric artifacts, while the light stimulation has a negligible effect on the electrodes at other positions. A comparative analysis reveals that the electrode at the lowest position (connected with Ch6) exhibits the highest photoelectric artifact amplitude. This is attributed to the tendency of light propagating in the core of the fiber to emit at the tip of the fiber, as indicated by our simulations. The resulting higher light intensity at the tip leads to stronger photoelectric artifacts for electrodes at lower positions. Furthermore, it is observed that the photoelectric artifacts strongly influence the local field

potential region (0.1-100 Hz) but have a negligible impact on multi-unit spike recordings (500-10000Hz). Power spectrum analysis of electric signal recording suggests that light-evoked artifacts mainly occur at frequencies of 10 Hz, 20 Hz, 30 Hz, and 40 Hz, matching the frequency of the stimulated light and its overtones (**fig. S12**). Using highpass filtering, it has been previously reported as a proposed strategy for mitigating artifacts in neural spike data (*40*). To further assess the separability of the artifacts from background noise, the signal-to-noise ratio (SNR) (*41*) of the photoelectric artifacts under various high-pass filters (from 100 Hz to 1000 Hz) was calculated (**fig. S13**), indicating that a 500 Hz high-pass filter can effectively inhibit the photoelectric artifacts to an amplitude comparable to the background noise level in neural activity recording.

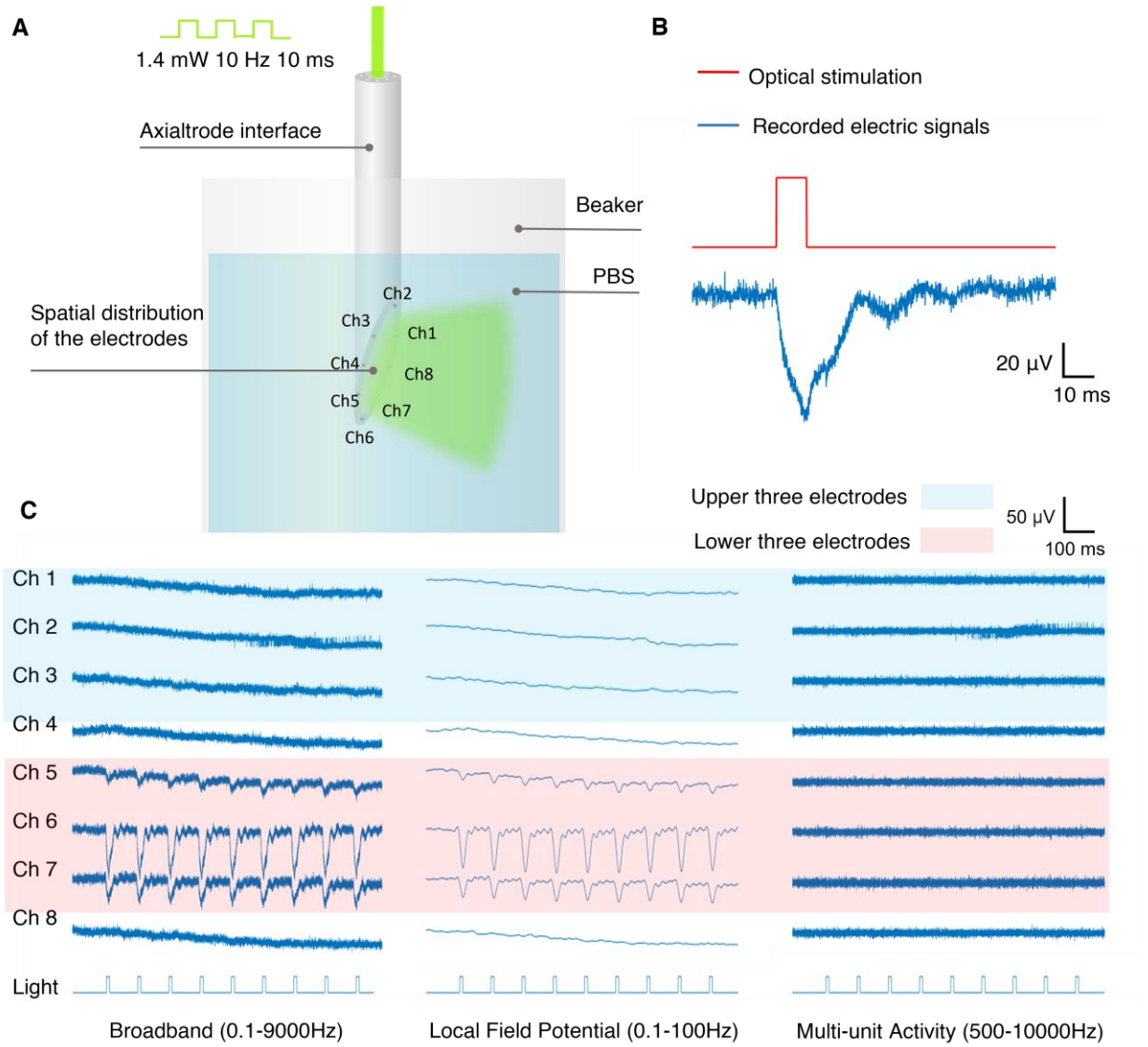

Fig. 3. Characterization of the photoelectric artifacts of the axialtrode. (A) Schematic representation of the experimental setup during the photoelectric artifacts characterization. **(B)** Temporal relationship between the optical stimulation and the raised photoelectric artifact pulse. **(C)** The recorded electric signal from all eight electrodes under illumination in broadband (1-9000 Hz), local field potential region (0.1-100 Hz), and multi-unit activity region (500-9000 Hz). The signals recorded from the upper three electrodes have been highlighted with blue shadow while the signals from the lower three electrodes have been marked with red shadow.

Awake *in vivo* theta wave recordings

Complex brain or spinal cord functions are underpinned by the synchronized activities of multiple neurons throughout different subregions of the brain. These neuronal ensembles are closely associated with various brain or spine rhythmic patterns (*42–44*). Among these, theta frequency oscillations, predominantly ranging from 4 to 10 Hz, are a critical rhythm observed within the hippocampal structure, serving as key indicators of cognitive processes and memory-related functions (*45*). These oscillatory activities are not only observable during conscious behaviors such as ambulation, leaping, or investigative olfactory actions but also during phases of rapid eye movement (REM) sleep (*46*, *47*). The genesis of these oscillations is traced back to the medial septum (MS), whose interneuronal network facilitates the synchronization of these rhythmic patterns to hippocampal areas (*48*). Although theta frequency oscillations are detectable in both hippocampal and cortical regions (*49*), it has been observed that the strength of cortical theta oscillations is typically less pronounced when compared to those in the hippocampus (*50*).

In this study, we conducted a proof-of-concept experiment to assess the depth-resolved recording capabilities of the axialtrodes by recording the theta oscillation intensity difference between the cortex and the hippocampus regions. The concept of the experiment is illustrated in **Fig. 4A**. We implanted the axialtrode with a tip angle of 15° into the brain of a mouse, positioning the bottom three electrodes within the hippocampal region and the top three electrodes in the cortical region. The span from the highest to the lowest electrode was measured to be ~900 µm. A representative 10-second segment of the recordings from all eight electrodes is presented in **Fig. 4B (**full recordings can be seen in **fig. S14)**, revealing a high degree of waveform similarity across the electrodes. Yet, when a bandpass filter (4-10 Hz) was applied to isolate theta oscillations, a notable difference emerged: the amplitudes of theta rhythms recorded by the bottom three electrodes (hippocampus) were consistently higher than those captured by the top three electrodes (cortex), as demonstrated in **fig. S15**. This observation was further substantiated by power spectrum analysis of the recordings from each electrode, illustrated in **Fig. 4C**. Here, the theta rhythms recorded by the hippocampus-located electrodes displayed markedly higher power compared to those recorded by the cortex-located electrodes. This correlation between our experimental findings and the established literature (*50*) validates the utility of our axialtrode for depth-specific neural activity recording. After the experiment, the implantation location was verified through an examination of the acute insertion footprint. Prior to implantation, the probe was coated with Hoechst dye to serve as a position marker under microscopic examination. **Figure 4D** reveals the fluorescent imaging of the tissue damage caused by the axialtrode implantation in dorsal-ventral direction of the mouse brain. It can be seen that the insertion footprint penetrated through the cortical layer and extended into the hippocampal region of the brain.

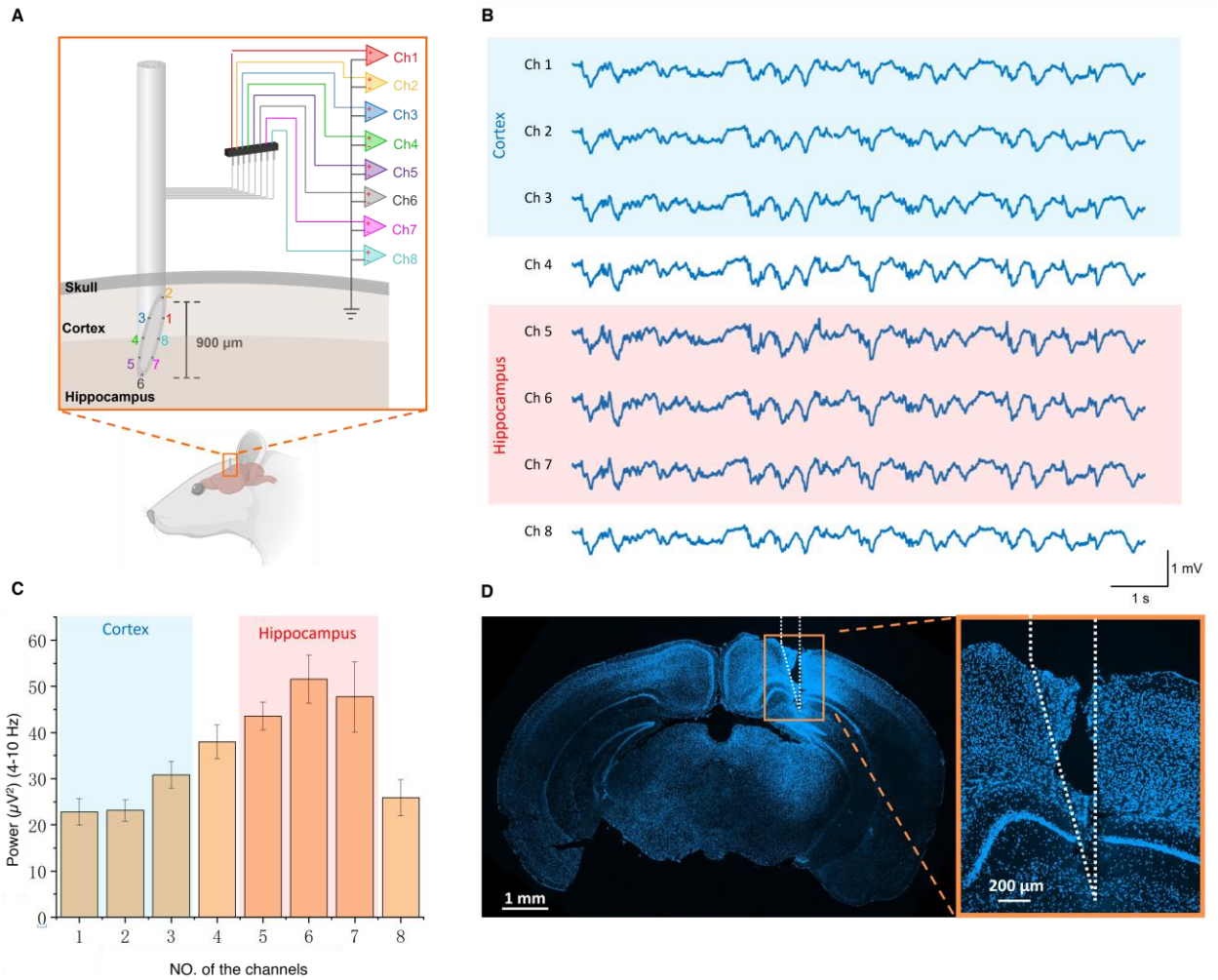

Fig. 4. Distinguishing the theta rhythms in the cortex and hippocampus using the developed axialtrode. (A) Illustration of the experimental concept: the axialtrode was implanted into the brain of a mouse with the lower three electrodes reaching the hippocampus region and the upper three electrodes touching the cortex tissue. The distance between the upmost and lowest electrode can be up to 900 μm. **(B)** The electric signals were recorded by the eight electrodes within 10 seconds. **(C)** Power of recorded theta wave by all the eight channels of the axialtrodes (electrodes location at the cortex and hippocampus were highlighted with light blue and red shadows, respectively). **(D)** Confocal fluorescent imaging of the insertion footprint in the dorsal-ventral direction of the mouse brain (magnification 10X).

In vivo axial optogenetics and electrophysiology

Optogenetics stands out for its exceptional cell-type specificity, providing a powerful means to explore functional connectivity across various brain regions with precise spatial and neuronal population selectivity (*51*). The integrated optical waveguide and electrodes in the axialtrodes make it an efficient tool for optogenetic applications. A proof-of-concept experiment was conducted to prove its utility in concurrent optical neural activity stimulation and electrophysiology recordings.

Movie S2 shows an animated rendition of the process of neural activity recording during an optogenetics experiment with the proposed axialtrode. After ChR2 was expressed in the visual cortex of a mouse brain (details of the genetic modification method of brain neurons have been described in **Materials and Methods**), an axialtrode with a tip angle of 15° was loaded into the

brain until the upmost electrodes (which correspond to channel 2 in the schematic in **Fig. 3A**) reached the surface of the visual cortex. Neural activities were stimulated by delivering blue light from a fiber-coupled LED. The output power at the tip of the fiber was measured to be 1.4 mW. The frequency and the pulse width were modulated by an LED driver (frequency: 10 Hz, pulse width: 10 ms), and TTL pulses from the stimulating signal were synchronized with the electrophysiology recording via the Intan RHX program. The resultant signals recorded by the eight electrodes are presented in **fig. S16** and **fig. S17**. A highpass filter (500 Hz) was applied to highlight the light-evoked neural activity, demonstrating that spikes triggered by optical stimulation can be recorded by all integrated electrodes (**fig. S18**). From a typical 1s recording illustrated in **Fig. 5A,** the signal from electrode 6 (Ch6) exhibited a lower amplitude than the rest possibly due to its further away position from the opsins (the virus was injected into the visual cortex). Interestingly, electrodes at upper positions (Ch1 to Ch3) captured typical tri-phasic axonal signals, while electrodes at lower positions (Ch6 and Ch7) recorded multi-unit activities with more complex 'w' shapes. Among the 6 channels that can record single-unit neural activities (Ch1-Ch5 and Ch8), we use principle component analysis on Ch1 (a representative single-unit activity recording channel) and found that two distinct spike clusters were identified, as shown in **Fig. 5B**. **Figure 5C** displays the superimposition and average shapes of these two spike types. The spike firing rate (SFR) was calculated by convolving the spikes' temporal locations with a Gaussian kernel (bin size: 0.2 s) as shown in **Fig. 5D**. The distinct SFRs of the two spike units (**Fig. 5E**) make it obvious that one of the clusters is strongly related to the light stimulation (cluster 2 in **Fig. 5C**), while the other appeared randomly throughout the recording (cluster 1 in **Fig. 5C**).

The study also investigated the effect of varying light pulse widths (10 ms, 20 ms, and 50 ms) on the evoked spikes. To do so, the spikes recorded by the eight channels immediately following light stimulation were compared (**Fig. 5F**). It was observed that a 10 ms light pulse evoked spikes with the highest amplitude, and the average amplitude of spikes collected by the eight electrodes decreased from 101.55 µV to 76.71 µV as the pulse width increased from 10 ms to 50 ms (**fig. S19 and table S1**). The results can be explained through the kinetic model of the ChR2 photocycle, which involves four kinetic intermediate states (P1, P2, P3, and P4) (*52*). It is hypothesized that the increase in photocurrents within the first 10 ms following light stimulation is attributed to the state transition from P1 to P3, where the open state time constants for transitions from P1 to P2 and P2 to P3 are 1 ms and 10 ms, respectively. However, when the duration of the light pulse exceeds 10 ms and reaches the P4 state, the desensitization leads to a reduction in photocurrents due to the inactivation of ChR2 (*53*).

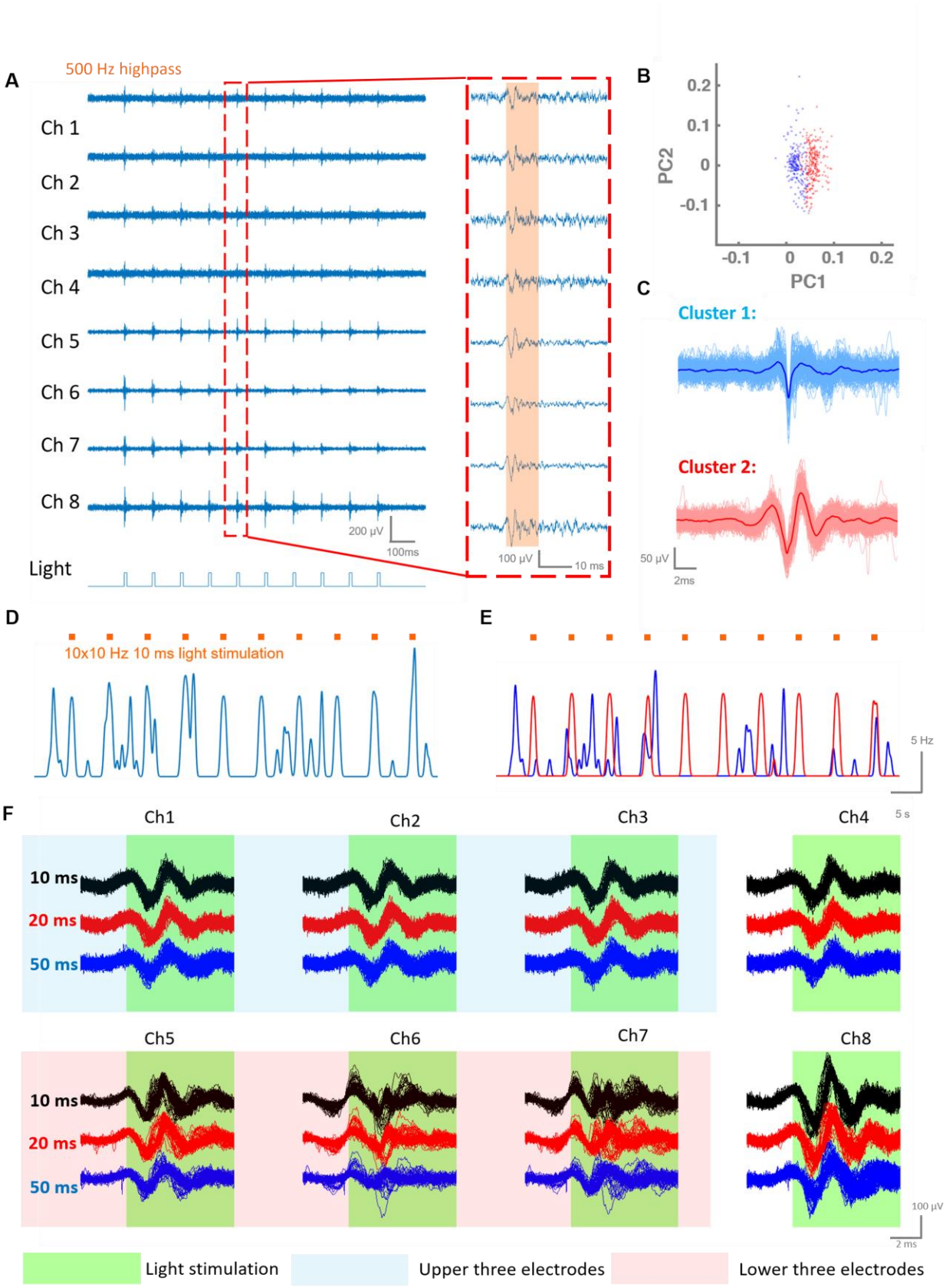
A
500 Hz highpass
Ch 1
Ch 2
Ch 3
Ch 4
Ch 5
Ch 6
Ch 7
Ch 8
Light
200 µV
100ms
100 µV
10 ms
B
PC2
PC1
0.2
0.1
0
-0.1
-0.1
0
0.1
0.2
C
Cluster 1:
Cluster 2:
50 µV
2ms
D
10x10 Hz 10 ms light stimulation
E
5 Hz
5 s
F
Ch1
Ch2
Ch3
Ch4
Ch5
Ch6
Ch7
Ch8
10 ms
20 ms
50 ms
100 µV
2 ms
Light stimulation
Upper three electrodes
Lower three electrodes

Fig. 5. Optogenetics experiment using the developed axialtrode for simultaneous optical stimulation and electrophysiology. (A) Neural activity recordings from the eight integrated electrodes. **(B)** Principal-component analysis (PCA) of the two units of spikes collected by Ch1. (**C**) Overlap and average action potential shape of the two clusters of spikes. **(D)** Spike firing rate recording by Ch1 under blue light stimulation. **(E)** Spike firing rate of the two clusters of spikes that were sorted by PCA under blue light stimulation. **(F)** Comparison of recorded neural activity shapes from the eight electrodes under the light simulation with different pulse widths (10 ms, 20 ms, 50 ms).

DISCUSSION

We have presented a new concept within implantable technologies defined as *axialtrode*, an implant constituted by a soft optical waveguide with integrated electrodes for optical neuromodulation and depth-resolved neural activity recording, respectively. The parameters of the device (including the diameter of the implant, the size of the optical waveguide, and the distance between the electrodes) can be easily adaptable and customized to different applications: by adjusting the thermal drawing process, the size of the optical waveguide is scalable to match the core of the optical patch cable that is connected to the light source, while the spatial distribution of the electrodes along the fiber length can be modified by adjusting the angle at the end facet of the polymer optical fiber.

To realize a distinct separation of electrodes along the axis of the polymer optical fibers to lift the degeneracy of layers during neural activity recordings, we introduced an angled tip by an in-house developed mechanical and fully repeatable process. Taking advantage of the softness of polymer materials, this process can be achieved simply by fixing the position of the optical fiber in the groove of the stainless steel block and sliding a blade along the side face of the block for the cutting of the angled fiber tip.

Compared with flat-end facet fiber-based implants, the sharpened tip of the axialtrode can not only reduce the tissue compression during the implantation but also avoid the buckling failure to increase the successful implantation rate (*54*, *55*). This is extremely important for the development of chronic, minimally invasive and reliable implants based on compliant materials (such as soft polymers) (*56*). Furthermore, another important advantage of the axialtrode is its reduced volume compared to flat-ended fibers that eventually leads to a suppressed inflammatory response in chronic implantations.

The capability of the proposed axialtrodes in terms of depth-resolved neural activity recording has been demonstrated through the differentiation of theta rhythms in the cortical and hippocampal regions of the brain. The theta wave's power, as recorded by the upper three electrodes situated in the cortical region, has a lower intensity compared to that recorded by the lower three electrodes in the hippocampal region of the axialtrode. In the optogenetics experiment, neural activities were recorded by all eight electrodes of the fiber-based implant, triggered by pulse light from an LED for ChR2 stimulation. Although preliminary *in vitro* experiments indicated potential photoelectric artifacts in the low-frequency range on the three electrodes nearest the optical waveguide's tip, these artifacts could be effectively eliminated by employing a high-pass filter during the action potential recordings.

The angled end facet of the axialtrodes showcased in this study, offers versatility beyond neural activity recording, extending to various depth-resolved neuromodulation or recording technologies. For example, incorporating MCs into the cladding of the polymer optical fibers enables depth-resolved pharmacological or chemical neuromodulation.

In summary, the degeneracy of brain layers introduced by interrogation of neurons with flat-end facet fibers has been lifted by introducing an angle at the tip of the fiber and integrating metal microwires into the fiber cladding MCs. The long distance between the uppermost and lowest electrodes can help neuroscientists gain a better understanding of the neural circuit dynamics across different brain depth regions.

MATERIALS AND METHODS

Thermal drawing of the PC/PMMA fibers

PC and PMMA polymer rods with a diameter of 25 mm were acquired from Goodfellow UK. The diameter of the PC rod was reduced to 10 mm by machining and a central hole with a diameter of 10.3 mm was drilled in the PMMA rod. Subsequently, eight hollow channels, each 4 mm in diameter, were drilled at the alternate end of the PMMA rod using a precision drill bit (HSCO, EJOT). This assembly, with the PC rod inserted into the PMMA tube, served as the structured preform for fiber fabrication. The fibers were drawn using an optical fiber draw tower facility at DTU Electro. The preform was fixed to the feeding system using a custom metal adaptor and then loaded into the furnace. The drawing process started after the temperature of the furnace reached 200 °C, causing the preform to form a drop. The speed of the feed system was set to 0.2 mm/min, while the fiber drawing speed was adjusted based on the target fiber diameter. Throughout the fiber fabrication, a laser diameter gauge was utilized to continuously monitor and ensure the stability of the fiber's diameter, which exhibited minimal fluctuation deviation (<1%) during several hundreds of meters.

Microscope image and near-field optical profiles

The PC/PMMA polymer optical fiber was cleaved using stainless steel blades (EHDIS) and the cross-section images of the fibers were captured in the transmission mode of a Zeiss Axioscan A1 microscope, equipped with an Axiocam 305 color camera.

To image the output light profile emanating from the PC/PMMA polymer optical fibers, a customized cage system was built to facilitate light coupling. Light emitted from a blue LED (M470L4, Thorlabs) or a red LED (M660L4, Thorlabs) was initially collimated through an aspheric lens (AL2520M-A, Thorlabs). The path of this collimated light was then adjusted using two broadband dielectric mirrors (BB1-E02, Thorlabs), each mounted on right-angle kinematic mounts (KCB1C/M, Thorlabs). The coupling into the fiber was achieved with another aspheric lens (AL2520M-A). The propagation light in the core of PC/PMMA was imaged by a digital microscope (AM7915MZT, Dino-Lite).

Development of the axialtrode scaffold

The 3D model of the axialtrode scaffold was designed using SolidWorks and subsequently fabricated using a high-resolution 3D printer (Sonic Mighty 8K, Phrozen), capable of achieving a resolution of 28 µm in the x-y plane (length and width) and 10 µm in the z-axis (thickness).

In the printing process, the build plate and resin vat were first installed in the printer. The Phrozen resin water was thoroughly mixed and then poured into the resin tank. The 3D model print file was transferred to the 3D printer via a USB disk to initiate the printing process. To minimize exposure to excessive UV light, the printer's plastic case was kept closed during the print. Upon completion of printing, the build plate was removed from the printer. A metal scraper was then used to carefully detach the printed axialtrode scaffolds from the build plate. The scaffolds were subsequently cleaned using Phrozen Wash Resin Cleaner and underwent final UV curing in a post-

curing chamber. Remarkably, this printing process allows for the production of up to 16 axialtrode scaffolds within one hour.

Ray tracing simulations and optical fiber illumination map in brain tissue

The simulation of light distribution for optical fibers with varying tip angles (90°, 45°, and 30°) was conducted using the ray-tracing software Zemax-OpticStudio. The layout of the model can be seen in **fig. S5**. The model consisted of two concentric cylinders representing a step-index optical fiber, with diameters of 200 µm and 400 µm, respectively. The refractive indices for the inner and outer cylinders were set at 1.58 (*19*) and 1.49 (*57*), corresponding to the properties of PC and PMMA materials. As ferrule patch cables with a numerical aperture of 0.39 (MR83L01, Thorlabs) (*58*, *59*) are commonly used to couple the light from a light source to the optical waveguide in the probes, accordingly, a point source with a divergence angle of 23° (matching the light emission angle of a patch cable with an NA of 0.39) and a wavelength of 470 nm was positioned adjacent to one end of the fiber in the simulation. Additionally, a homogenous rectangular volume, representing brain tissue, was placed at the opposite end of the fiber. The refractive index of the brain tissue volume was set as 1.36 and its scattering properties were modeled using a Henyey-Greenstein scattering function with a mean free path of 0.04895 mm, an anisotropy value of 0.9254, and a transmission of 0.9989 (*60*). The spatial power distribution at the end of the fiber was recorded by raster scanning a square detector (dimension: 10x10 µm) in the x-z plate. The resulting light intensity distribution was mapped in MATLAB. An interpolation algorithm was applied to enhance the resolution of the resultant image.

Fiber loss measurement

The transmission properties of the fabricated fibers were characterized by measuring the propagation loss using the standard cut-back method. A high-power supercontinuum fiber laser (SuperK Extreme, NKT Photonics A/S) covering a wide wavelength range from 400 nm to 2400 nm was utilized as the light source. Due to the necessity of high pump power for generating broadband supercontinuum light, resulting in a total average power exceeding 5 W, a variable neutral density filter at the output of the laser was employed to reduce the launch power to ~100 mW, thereby preventing potential thermal damage to the end facets of the fiber. In addition, a beam trap (BT610/M, Thorlabs) was used to safely capture any residual reflected light. The light from the laser source was then efficiently coupled into the core of the polymer optical fibers using an achromatic objective lens with a 10x magnification and the output transmitted spectrum was measured using a spectrometer (CCS200, Thorlabs).

Impedance spectroscopy measurements

For the electrochemical impedance spectroscopy analysis, a chemical impedance analyzer (IM3590, Hioki) was employed in a three-terminal setup. In this configuration, a tungsten microwire, coiled around a rod, functioned as the counter electrode. An Ag/AgCl electrode was chosen as the reference electrode, and the electrodes integrated into the angled tip fiber devices served as the working electrodes. All electrodes were immersed in a phosphate-buffered saline (PBS) solution, which acted as the electrolytic medium. The impedance properties of the fiber devices were then meticulously measured across a frequency range spanning from 1 Hz to 10 kHz.

Electrophysiology recordings

Electrophysiological data acquisition was conducted using the RHS Stim/Recording System from Intan Technologies, which comprises an RHS Stim/Recording Headstage, an RHS Stim/Recording Controller, and a Stim SPI Interface Cable. The electrophysiology setup is detailed in **fig. S10** A

self-made adaptor was developed for delivering the electrical signals from eight pins in the neural interface device to the RHS stim/recording head stage. All the results can be visualized by the RHX Data Acquisition Software during the *in vivo* experiment. For all the recordings, the sampling rate was set at 20 kHz.

Optical Stimulation

Pulsed light at the wavelength of 470 nm (10Hz) with various pulse widths for optical stimulation was generated from a fiber-coupled LED (M470L4, Thorlabs) and driven by an LED driver (DC2200, Thorlabs) with internal modulation of square waveforms. The power output at the fiber tip was calibrated to 1.4 mW. For synchronizing the temporal profiles of optical stimulation pulses with the electrical signals, the LED driver was integrated with the Intan data acquisition system, enabling cohesive data communication. Identical optical stimulation parameters were employed in both the photoelectric artifact and optogenetic experiments to facilitate direct comparison and analysis of the results.

Preparation of the brain slices for the illumination map characterization

The procedure to prepare the fixed brain slices presented below is approved by the Animal Experiments Inspectorate under the Danish Ministry of Food, Agriculture, and Fisheries, and all procedures adhere to the European guidelines for the care and use of laboratory animals, EU directive 2010/63/EU.

A C57BL/6 mouse was anesthetized by the intraperitoneal injection of 0.01mL sodium pentobarbital (50 mg/kg). Once deep anesthesia was successfully achieved, the chest of the animal was opened in order to expose the heart. A needle, attached to a peristaltic pump (minipuls3, Gilson) via a catheter, was carefully inserted into the left ventricle of the heart before a small incision at the vena cava inferior was cut with fine surgery scissors to serve as the outlet of the blood during the perfusion. After 30 mL of 1X phosphate-buffered saline and 30 mL 4% paraformaldehyde (PFA) were perfused in succession, the animal was decapitated with a guillotine. The brain was dissected out and immersed in ice-cold 4% paraformaldehyde (PFA). The brain samples were incubated in PFA overnight and then with 30% sucrose solution for 2 days. The fixed brain was then cut into slices with a mouse brain matrice (coronal, 0.5mm cut, AgnTho's). To prevent any movement of the brain during the cutting process, 3% (w/v) agarose gel was used to fill all the gaps between the stainless steel matrice and the brain tissue. Brain slices with a thickness of 500 µm were cut for measuring the illumination map of the developed axialtrodes.

Ethical approval and animal handling for *in vivo* experiments

Animal experiments were conducted according to the United Kingdom Animal (Scientific Procedures) Act 1986, and approved by the Animals in Scientific Research Unit at the Home Office. Animals were housed in a 12 h/12 h dark/light cycle, and food and water were given ad libitum. The animals were group-housed prior to headbar surgery, but after this, animals were individually housed.

Virus injection

All following surgical procedures described were conducted aseptically. The C57BL/6 mice were anesthetized using isoflurane (988–3245, Henry Schein) followed by head shaving and skin disinfection. Then, the heads of the animals were fixed in a stereotaxic frame (David Kopf Instruments) by ear bars while a heating pad was used to maintain their body temperature. The body of the animal was covered with a sterile drape to minimize the temperature fluctuation during the surgery. Viscotears were applied (Bausch + Lomb). Buprenorphine (0.5 mg per/kg, Ceva) and

Metacam (15 mg/kg, Boehringer) were subcutaneously injected for pain relief. After the animal lost its pedal reflex response, the skin on the top of the head was cut to expose the skull with a surgical scalpel, and a surgery drill was used to expose the cortex surface in the left hemisphere of the mouse brain for virus injection. 1uL of AAV9-pAAV-CaMKIIa-hChR2(H134R)-EYFP (Addgene) was injected into the visual cortex (coordinates: anteroposterior: -2.3 mm, mediolateral: 1.8 mm dorsoventral: 0.3 and 0.55 mm) using a stereotaxic frame at the speed of 75 nL/min.

Surgeries for head bar attachment

Following injection of virus, a plate on the surface of the skull for the fixation of the animal's brain with the head bar on the Neurostar system during subsequent awake in vivo experiments. After the skull was cleaned and dried, a small hole on the left hemisphere of the animal's head was created by drilling (RA1 008, Henry Schein) for a metal support screw (00-96×3-32, Plastics One). The head plate was attached and strengthened using vetbond (1469SB, 3M), and dental cement, respectively flowed by the covering of the skull with silicone (Kwik-Cast, WPI). Saline was administered prior to recovery or every 45 min depending on the length of surgery.

Mice were checked daily to ensure recovery. After at least 5 days of recovery, habituation was performed by placing the mouse in the Neurotar frame for increasing periods of time (15–60 min) over several days.

Craniotomy for the axialtrode implantation

A craniotomy was performed on the day of the in vivo experiment. After the anesthesia using isoflurane and the administration of pain medication and intramuscular dexamethasone (1 mg/kg, intramuscular; 7247104, MSD Animal Health), A large (2x2 mm^2) craniotomy was performed above the somatosensory and visual cortex on the left hemisphere. Cold-buffered saline was continually applied to the craniotomies throughout the experiment. Then, the exposed dura was covered with buffered saline, a piece of sterilized Sylgard (~200 μm thick), and a silicone layer.

After two hours, the head of the animal was fixed to the Neurotar frame and the craniotomies were exposed by removal of the silicone and Sylguard layers. The tip of the axialtrode was lowered using a micromanipulator into the visual cortex or the hippocampus of the animal for neural stimulation or recordings. After the *in vivo* experiment (1-2hrs), sodium pentobarbital was administered intraperitoneally to humanely cull the animal prior to extraction of the brain for post-hoc analysis.

Chronic biocompatibility evaluation of the axialtrodes

An immunohistochemistry experiment was carried out to evaluate the biocompatibility difference between the axialtrodes and conventional flat end-facet optical fibers. During probe implantation, a stereotaxic robot and drill were used to make two small holes in the skull in each hemisphere of mice (anterioposterior -2 mm, mediolateral 1.5 mm, dorsoventral 2 mm from dura mater). The axialtrodes were implanted in the left hemisphere while the fiber with the same diameter but a flat end-facet was implanted in the right hemisphere. The skull was then sealed by cyanoacrylate adhesive and dental cement. After the surgery, the mice were orally treated with buprenorphine (0.2 mg mixed with 1 g Nutella) every 12 hours for three days. Furthermore, Carprofen (5 mg/kg) was administered subcutaneously every 12 hours for 5 days. The conditions of the animals were monitored 2–3 times per day over the first 3 days and once daily for the following week.

Four weeks after device implantation, the mice were perfused and their brains were removed, and cryoprotected with the same procedure as described above when getting brain slices for the

illumination map measurement. A cryostat (CM3050S, Leica) was used to slice the brain with a thickness of 50 µm. After being washed in PBS and preincubated in 0.3% Triton X-100 (PBST) for 15 mins, the slices were then incubated in a blocking solution consisting of 3% bovine serum albumin (BSA) for 1 h at 25 °C. Primary antibodies (1:1000 dilution, rabbit polyclonal, Wako 019-19741) were applied to the slice for overnight incubation at 4 °C. Afterwards, the slices were washed three times with 0.1 % PBST. Then, secondary antibodies (goat anti-rabbit, Alexa Fluor 488,Invitrogen) together with 4',6-Diamidino-2-Phenylindole, Dihydrochloride (DAPI, Invitrogen, D1306) was applied at a concentration of 1:1000. After the incubation in dark room for 1h at 25 °C, the slices were rewashed three times with 0.1 % PBST. Finally, the glass slides were mounted using DAKO mounting medium and imaged using a Zeiss Axioscan Z1 microscope (×10 magnification).

Images were loaded at full resolution in Zeiss ZEN software and two different square ROIs with a dimension of 500 x 500 µm centered around the tip of the axialtrodes and the flat end-facet fibers were cropped. After discarding the images found to be out of focus or presenting too large artifacts, a threshold was applied to eliminate the signal from out-of-plane cells, and the maximum pixel value was adjusted to increase contrast. The analysis of the images was achieved by the Fiji open-source image processing package, based on ImageJ2. After the marker and DAPI channels were separated, the mean fluorescence intensity of the Iba-1 marker was calculated.

Data processing

The data processing and analysis were performed in the Matlab 2022b suite.

The SNR was calculated by dividing the median amplitude of all spike events surpassing the threshold by the threshold value itself (*41*). Here the threshold for spike detection was set as (*61*)

$$Thr = a * median(\frac{|x|}{0.6745})$$

where $|x|$ represents the amplitude of the high-passed data, and a represents a factor for different threshold levels. This factor was set to a = 3 for the standard procedure and was varied between 2 and 4 for an iterative procedure. We use a = 3 in this work.

In the PCA analysis, the principal component coefficients are obtained by the singular value decomposition (SVD) algorithm. The clusters were sorted based on fitting the Gaussian mixture model to the data. The Gaussian mixture model was initialized with the k-means++ algorithm and used diagonal and identical covariance matrices to fit the data.

REFERENCES AND NOTES

1. H. Adesnik, L. Abdeladim, Probing neural codes with two-photon holographic optogenetics. *Nat Neurosci* **24**, 1356–1366 (2021).
2. A. Gerits, W. Vanduffel, Optogenetics in primates: a shining future? *Trends in Genetics* **29**, 403–411 (2013).
3. Y. Mei, F. Zhang, Molecular Tools and Approaches for Optogenetics. *Biological Psychiatry* **71**, 1033–1038 (2012).
4. N. Zheng, Y. Jiang, S. Jiang, J. Kim, G. Chen, Y. Li, J.-X. Cheng, X. Jia, C. Yang, Multifunctional Fiber-Based Optoacoustic Emitter as a Bidirectional Brain Interface. *Advanced Healthcare Materials* **n/a**, 2300430.
5. B. Spagnolo, A. Balena, R. T. Peixoto, M. Pisanello, L. Sileo, M. Bianco, A. Rizzo, F. Pisano, A. Qualtieri, D. D. Lofrumento, F. De Nuccio, J. A. Assad, B. L. Sabatini, M. De Vittorio, F. Pisanello, Tapered fibertrodes for optoelectrical neural interfacing in small brain volumes with reduced artefacts. *Nat. Mater.* **21**, 826–835 (2022).

6. F. Pisanello, L. Sileo, I. A. Oldenburg, M. Pisanello, L. Martiradonna, J. A. Assad, B. L. Sabatini, M. De Vittorio, Multipoint-Emitting Optical Fibers for Spatially Addressable In Vivo Optogenetics. *Neuron* **82**, 1245–1254 (2014).
7. S. Royer, B. V. Zemelman, M. Barbic, A. Losonczy, G. Buzsáki, J. C. Magee, Multi-array silicon probes with integrated optical fibers: light-assisted perturbation and recording of local neural circuits in the behaving animal. *European Journal of Neuroscience* **31**, 2279–2291 (2010).
8. A. V. Kravitz, S. F. Owen, A. C. Kreitzer, Optogenetic identification of striatal projection neuron subtypes during in vivo recordings. *Brain Research* **1511**, 21–32 (2013).
9. F. Pisanello, G. Mandelbaum, M. Pisanello, I. A. Oldenburg, L. Sileo, J. E. Markowitz, R. E. Peterson, A. Della Patria, T. M. Haynes, M. S. Emara, B. Spagnolo, S. R. Datta, M. De Vittorio, B. L. Sabatini, Dynamic illumination of spatially restricted or large brain volumes via a single tapered optical fiber. *Nature Neuroscience* **20**, 1180–1188 (2017).
10. G. Buzsáki, E. Stark, A. Berényi, D. Khodagholy, D. R. Kipke, E. Yoon, K. D. Wise, Tools for Probing Local Circuits: High-Density Silicon Probes Combined with Optogenetics. *Neuron* **86**, 92–105 (2015).
11. D. Kuzum, H. Takano, E. Shim, J. C. Reed, H. Juul, A. G. Richardson, J. de Vries, H. Bink, M. A. Dichter, T. H. Lucas, D. A. Coulter, E. Cubukcu, B. Litt, Transparent and flexible low noise graphene electrodes for simultaneous electrophysiology and neuroimaging. *Nat Commun* **5**, 5259 (2014).
12. F. Wu, E. Stark, P. C. Ku, K. D. Wise, G. Buzsáki, E. Yoon, Monolithically Integrated μLEDs on Silicon Neural Probes for High-Resolution Optogenetic Studies in Behaving Animals. *Neuron* **88**, 1136–1148 (2015).
13. Y. Zhang, X. Wu, R. A. Vadlamani, Y. Lim, J. Kim, K. David, E. Gilbert, Y. Li, R. Wang, S. Jiang, A. Wang, H. Sontheimer, D. F. English, S. Emori, R. V. Davalos, S. Poelzing, X. Jia, Submillimeter Multifunctional Ferromagnetic Fiber Robots for Navigation, Sensing, and Modulation. *Advanced Healthcare Materials* **n/a**, 2300964.
14. A. L. Chin, S. Jiang, E. Jang, L. Niu, L. Li, X. Jia, R. Tong, Implantable optical fibers for immunotherapeutics delivery and tumor impedance measurement. *Nat Commun* **12**, 5138 (2021).
15. S. Jiang, D. C. Patel, J. Kim, S. Yang, W. A. Mills, Y. Zhang, K. Wang, Z. Feng, S. Vijayan, W. Cai, A. Wang, Y. Guo, I. F. Kimbrough, H. Sontheimer, X. Jia, Spatially expandable fiber-based probes as a multifunctional deep brain interface. *Nat Commun* **11**, 6115 (2020).
16. P. Anikeeva, A. S. Andalman, I. Witten, M. Warden, I. Goshen, L. Grosenick, L. A. Gunaydin, L. M. Frank, K. Deisseroth, Optetrode: a multichannel readout for optogenetic control in freely moving mice. *Nat Neurosci* **15**, 163–170 (2012).
17. S. Park, Y. Guo, X. Jia, H. K. Choe, B. Grena, J. Kang, J. Park, C. Lu, A. Canales, R. Chen, Y. S. Yim, G. B. Choi, Y. Fink, P. Anikeeva, One-step optogenetics with multifunctional flexible polymer fibers. *Nature Neuroscience* **20**, 612–619 (2017).
18. S. Park, G. Loke, Y. Fink, P. Anikeeva, Flexible fiber-based optoelectronics for neural interfaces. *Chemical Society Reviews* **48**, 1826–1852 (2019).
19. A. Canales, X. Jia, U. P. Froriep, R. A. Koppes, C. M. Tringides, J. Selvidge, C. Lu, C. Hou, L. Wei, Y. Fink, P. Anikeeva, Multifunctional fibers for simultaneous optical, electrical and chemical interrogation of neural circuits in vivo. *Nature Biotechnology* **33**, 277–284 (2015).
20. S. Park, H. Yuk, R. Zhao, Y. S. Yim, E. W. Woldeghebriel, J. Kang, A. Canales, Y. Fink, G. B. Choi, X. Zhao, P. Anikeeva, Adaptive and multifunctional hydrogel hybrid probes for long-term sensing and modulation of neural activity. *Nat Commun* **12**, 3435 (2021).
21. M. Meneghetti, J. Kaur, K. Sui, J. F. Sørensen, R. W. Berg, C. Markos, Soft monolithic infrared neural interface for simultaneous neurostimulation and electrophysiology. *Light Sci Appl* **12**, 127 (2023).
22. M. Meneghetti, F. Gudmundsen, N. S. Jessen, K. Sui, C. Baun, M. Palner, C. Markos, Mapping whole brain effects of infrared neural stimulation with positron emission tomography. *Imaging Neuroscience* **1**, 1–17 (2023).
23. P. Xu, A. Chen, Y. Li, X. Xing, H. Lu, Medial prefrontal cortex in neurological diseases. *Physiological Genomics* **51**, 432–442 (2019).
24. A. Bonaccini Calia, E. Masvidal-Codina, T. M. Smith, N. Schäfer, D. Rathore, E. Rodríguez-Lucas, X. Illa, J. M. De la Cruz, E. Del Corro, E. Prats-Alfonso, D. Viana, J. Bousquet, C. Hébert, J. Martínez-Aguilar,

J. R. Sperling, M. Drummond, A. Halder, A. Dodd, K. Barr, S. Savage, J. Fornell, J. Sort, C. Guger, R. Villa, K. Kostarelos, R. C. Wykes, A. Guimerà-Brunet, J. A. Garrido, Full-bandwidth electrophysiology of seizures and epileptiform activity enabled by flexible graphene microtransistor depth neural probes. *Nat. Nanotechnol.* **17**, 301–309 (2022).
25. L. Sileo, S. H. Bitzenhofer, B. Spagnolo, J. A. Pöpplau, T. Holzhammer, M. Pisanello, F. Pisano, E. Bellistri, E. Maglie, M. De Vittorio, P. Ruther, I. L. Hanganu-Opatz, F. Pisanello, Tapered Fibers Combined With a Multi-Electrode Array for Optogenetics in Mouse Medial Prefrontal Cortex. *Frontiers in Neuroscience* **12** (2018).
26. M. Chen, Z. Wang, Q. Zhang, Z. Wang, W. Liu, M. Chen, L. Wei, Self-powered multifunctional sensing based on super-elastic fibers by soluble-core thermal drawing. *Nature Communications* **12**, 1416 (2021).
27. J. M. Cariou, J. Dugas, L. Martin, P. Michel, Refractive-index variations with temperature of PMMA and polycarbonate. *Appl. Opt., AO* **25**, 334–336 (1986).
28. C. H. C. Keck, N. J. Rommelfanger, Z. Ou, G. Hong, Bioinspired nanoantennas for opsin sensitization in optogenetic applications: a theoretical investigation. *Multifunct. Mater.* **4**, 024002 (2021).
29. C. M. Ambrosi, E. Entcheva, "Optogenetic Control of Cardiomyocytes via Viral Delivery" in *Cardiac Tissue Engineering: Methods and Protocols*, M. Radisic, L. D. Black III, Eds. (Springer, New York, NY, 2014; https://doi.org/10.1007/978-1-4939-1047-2_19)*Methods in Molecular Biology*, pp. 215–228.
30. S. Chen, Optical modulation goes deep in the brain. *Science* **365**, 456–457 (2019).
31. Z. Zhou, Z. Wang, W. Huang, Y. Cui, H. Li, M. Wang, X. Xi, S. Gao, Y. Wang, Towards high-power mid-IR light source tunable from 3.8 to 4.5 µm by HBr-filled hollow-core silica fibres. *Light Sci Appl* **11**, 15 (2022).
32. A. Stefani, W. Yuan, C. Markos, O. Bang, Narrow Bandwidth 850-nm Fiber Bragg Gratings in Few-Mode Polymer Optical Fibers. *IEEE Photonics Technology Letters* **23**, 660–662 (2011).
33. A. Fasano, G. Woyessa, P. Stajanca, C. Markos, A. Stefani, K. Nielsen, H. K. Rasmussen, K. Krebber, O. Bang, Fabrication and characterization of polycarbonate microstructured polymer optical fibers for high-temperature-resistant fiber Bragg grating strain sensors. *Opt. Mater. Express, OME* **6**, 649–659 (2016).
34. A. Tanaka, H. Sawada, T. Takoshima, N. Wakaisuki, "New Plastic Optical Fiber With Polycarbonate Core And Fluorescence-Doped Fiber For High Temperature Use" in *Fiber Optic Systems for Mobile Platforms* (SPIE, 1987; https://www.spiedigitallibrary.org/conference-proceedings-of-spie/0840/0000/New-Plastic-Optical-Fiber-With-Polycarbonate-Core-And-Fluorescence-Doped/10.1117/12.942588.full)vol. 0840, pp. 19–28.
35. T. Y. T. Yamashita, K. K. K. Kamada, Intrinsic Transmission Loss of Polycarbonate Core Optical Fiber. *Jpn. J. Appl. Phys.* **32**, 2681 (1993).
36. G. Dijk, A. L. Rutz, G. G. Malliaras, Stability of PEDOT:PSS-Coated Gold Electrodes in Cell Culture Conditions. *Advanced Materials Technologies* **5**, 1900662 (2020).
37. B. C. Brusso, A Brief History of the Energy Conversion of Light [History]. *IEEE Industry Applications Magazine* **25**, 8–13 (2019).
38. A. Yazdan-Shahmorad, D. B. Silversmith, V. Kharazia, P. N. Sabes, Targeted cortical reorganization using optogenetics in non-human primates. *eLife* **7**, e31034 (2018).
39. S. Mikulovic, S. Pupe, H. M. Peixoto, G. C. D. Nascimento, K. Kullander, A. B. L. Tort, R. N. Leão, On the photovoltaic effect in local field potential recordings. *NPh* **3**, 015002 (2016).
40. T. D. Y. Kozai, A. L. Vazquez, Photoelectric artefact from optogenetics and imaging on microelectrodes and bioelectronics: new challenges and opportunities. *J. Mater. Chem. B* **3**, 4965–4978 (2015).
41. E. Drebitz, B. Schledde, A. K. Kreiter, D. Wegener, Optimizing the Yield of Multi-Unit Activity by Including the Entire Spiking Activity. *Front. Neurosci.* **13** (2019).
42. W. A. MacKay, Synchronized neuronal oscillations and their role in motor processes. *Trends in Cognitive Sciences* **1**, 176–183 (1997).
43. C. Puentes-Mestril, J. Roach, N. Niethard, M. Zochowski, S. J. Aton, How rhythms of the sleeping brain tune memory and synaptic plasticity. *Sleep* **42**, zsz095 (2019).
44. H. Lindén, P. C. Petersen, M. Vestergaard, R. W. Berg, Movement is governed by rotational neural dynamics in spinal motor networks. *Nature* **610**, 526–531 (2022).

45. W. Klimesch, EEG alpha and theta oscillations reflect cognitive and memory performance: a review and analysis. *Brain Research Reviews* **29**, 169–195 (1999).
46. E. V. Lubenov, A. G. Siapas, Hippocampal theta oscillations are travelling waves. *Nature* **459**, 534–539 (2009).
47. K. Semba, B. R. Komisaruk, Phase of the theta wave in relation to different limb movements in awake rats. *Electroencephalography and Clinical Neurophysiology* **44**, 61–71 (1978).
48. L. L. Colgin, Mechanisms and Functions of Theta Rhythms. *Annual Review of Neuroscience* **36**, 295–312 (2013).
49. G. Buzsáki, Theta Oscillations in the Hippocampus. *Neuron* **33**, 325–340 (2002).
50. G. C. Sih, K. K. Tang, Sustainable time and stability of hippocampal and cortical EEG theta waves. *Theoretical and Applied Fracture Mechanics* **62**, 1–14 (2012).
51. K. Deisseroth, Optogenetics. *Nat Methods* **8**, 26–29 (2011).
52. C. Bamann, T. Kirsch, G. Nagel, E. Bamberg, Spectral Characteristics of the Photocycle of Channelrhodopsin-2 and Its Implication for Channel Function. *Journal of Molecular Biology* **375**, 686–694 (2008).
53. A. Erofeev, E. Gerasimov, A. Lavrova, A. Bolshakova, E. Postnikov, I. Bezprozvanny, O. L. Vlasova, Light Stimulation Parameters Determine Neuron Dynamic Characteristics. *Applied Sciences* **9**, 3673 (2019).
54. A. M. Stiller, M. A. González-González, J. M. Boothby, S. E. Sherman, J. Benavides, M. Romero-Ortega, J. J. Pancrazio, B. J. Black, Mechanical considerations for design and implementation of peripheral intraneural devices. *J. Neural Eng.* **16**, 064001 (2019).
55. K. Sui, M. Meneghetti, R. W. Berg, C. Markos, Optoelectronic and mechanical properties of microstructured polymer optical fiber neural probes. *Optics Express* **31**, 21563–21575 (2023).
56. A. A. Sharp, A. M. Ortega, D. Restrepo, D. Curran-Everett, K. Gall, In Vivo Penetration Mechanics and Mechanical Properties of Mouse Brain Tissue at Micrometer Scales. *IEEE Transactions on Biomedical Engineering* **56**, 45–53 (2009).
57. L.-H. Lee, W.-C. Chen, High-Refractive-Index Thin Films Prepared from Trialkoxysilane-Capped Poly(methyl methacrylate)−Titania Materials. *Chem. Mater.* **13**, 1137–1142 (2001).
58. I. Trujillo-Pisanty, C. Sanio, N. Chaudhri, P. Shizgal, Robust optical fiber patch-cords for in vivo optogenetic experiments in rats. *MethodsX* **2**, 263–271 (2015).
59. Y. Bouchekioua, I. Tsutsui-Kimura, H. Sano, M. Koizumi, K. F. Tanaka, K. Yoshida, Y. Kosaki, S. Watanabe, M. Mimura, Striatonigral direct pathway activation is sufficient to induce repetitive behaviors. *Neuroscience Research* **132**, 53–57 (2018).
60. E. Maglie, M. Pisanello, F. Pisano, A. Balena, M. Bianco, B. Spagnolo, L. Sileo, B. L. Sabatini, M. D. Vittorio, F. Pisanello, Ray tracing models for estimating light collection properties of microstructured tapered optical fibers for optical neural interfaces. *Opt. Lett., OL* **45**, 3856–3859 (2020).
61. R. Q. Quiroga, Z. Nadasdy, Y. Ben-Shaul, Unsupervised Spike Detection and Sorting with Wavelets and Superparamagnetic Clustering. *Neural Computation* **16**, 1661–1687 (2004).

Acknowledgments: The authors would like to thank Dr. Yazhou Wang for assistance in the optical characterization of the axialtrodes.

Funding: This work was supported by Lundbeck Foundation R276- 2018-869 Multi-BRAIN and R380-2021-1171.

Author contributions: Conceptualization and experiment design: K.S. and C.M. Axialtrode fabrication: K.S. and M.M. Axialtrode characterization: K.S. Brain slice for illumination map measurement: K.S. and G.L. Immunohistochemistry experiment: K.S. and G.L. Surgery of the in vivo experiment: N.C. and D.R. Electrophysiology recording: K.S., N.C. and D.R. Data analysis: K.S. and M.M. Funding acquisition: C.M., M.M., R.B. and R.W. Supervision: C.M., R.B. and

R.W. Draft writing: K.S. Draft edited by all authors. All authors approved the final version of the manuscript.

Competing interests: The authors declare that they have no competing interests.

Data and materials availability: All data needed to evaluate the conclusions in the paper are present in the paper and/or the Supplementary Materials. Additional data related to this paper may be requested from the authors.

Supplementary Materials

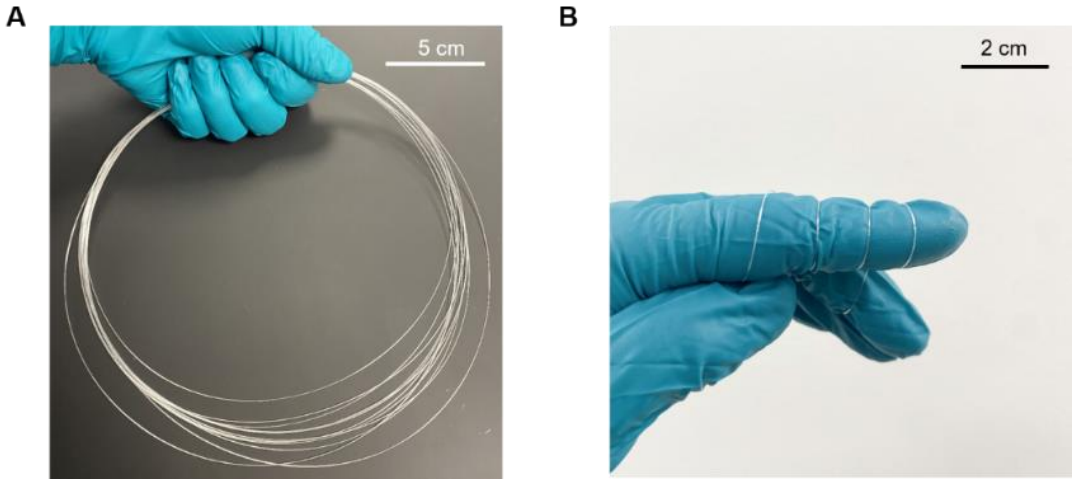

Fig. S1. The drawn PC/PMMA polymer optical fibers. (A) Tens of meters of polymer optical fiber were produced with the thermal drawing method. **(B)** The fibers have high flexibility, allowing them to be wrapped around a finger without breaking.

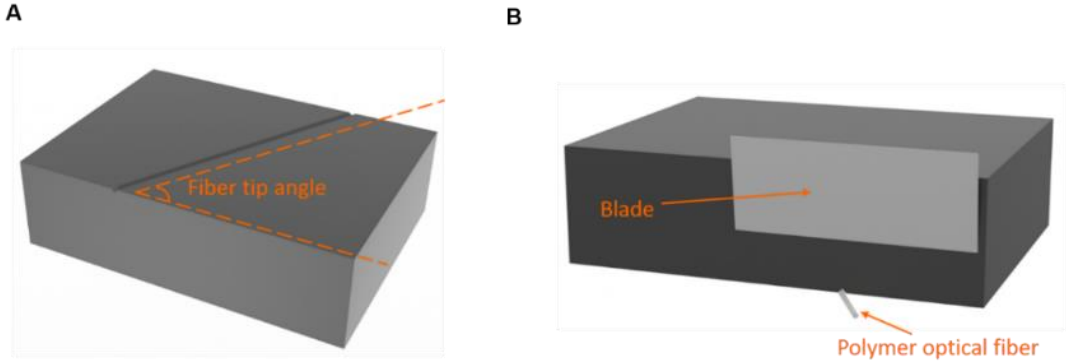

Fig. S2. Mechanical cutting method for introducing an angle at the tip of optical fibers. (A) The groove was machined at one surface of a stainless steel block. The angle between the groove and the edge of the block was chosen based on the target fiber tip angle. **(B)** The polymer optical fiber was placed in the groove and the cutting was achieved by sliding the blade down along the side face of the stainless steel block.

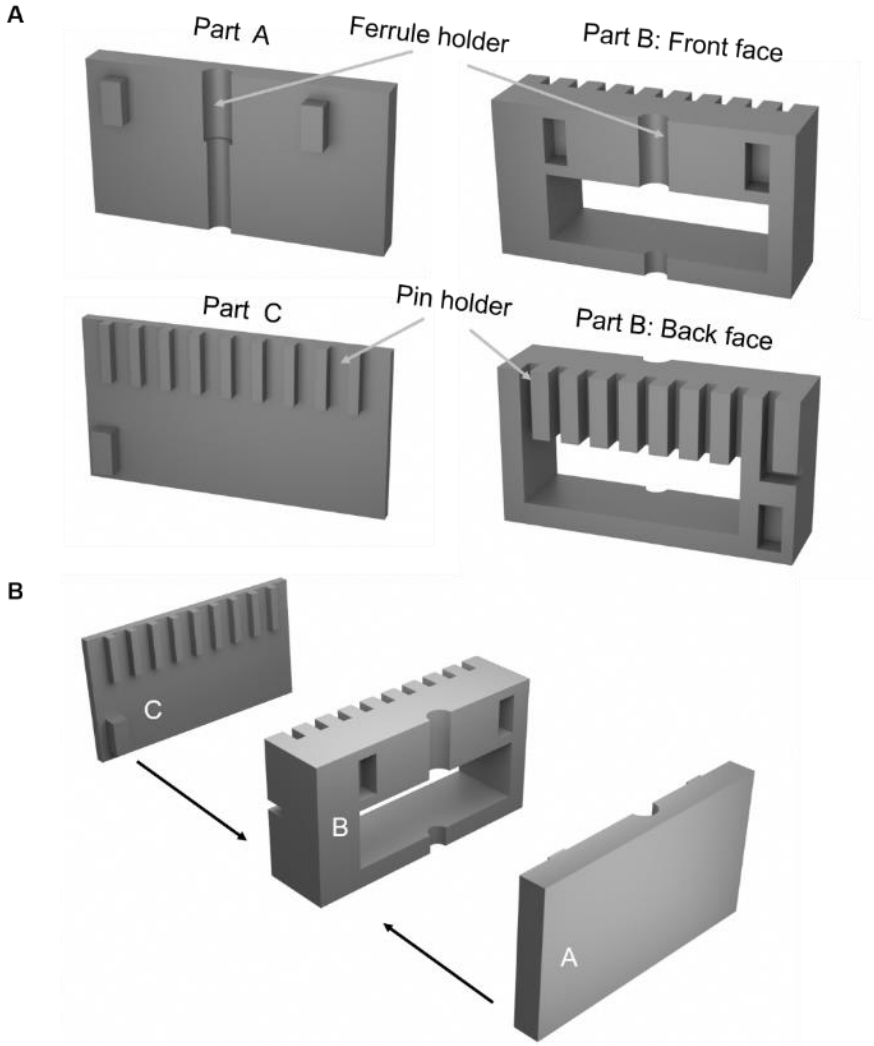

Fig. S3. The 3D printed scaffold for the axialtrode. (A) The detailed structures of the 3 parts in the scaffold. The assembling of parts A and B can fix the position of the ferrule on the axialtrode while the assembling of parts B and C can fix the position of the eight tungsten wires and the grounding wire to a 1.27 mm pin header (9 pins in total). **(B)** A schematic of the assembling configuration of the three parts of the axialtrode scaffold. Instead of connecting the metal wires with the pins by soldering, we achieved a robust electrode-pin connectorization by the interference fit between pin holders in Part B and Part C. In the assembly process, firstly, the position of the ferrule attached axialtrode was fixed by assembling part A to the front face of part B. Secondly, a tungsten wire, which would work as the grounding wire in the in vivo test, was placed into the rightmost slot in the back face of Part B, followed by the placing of the eight tungsten wires in the axialtrode to the rest eight slots in the back face of Part B. Then, a 9-pin header was inserted into the 9 slots in the back face of Part B. Finally, Part C was assembled to the back face of Part B. The interference fit between the pin holders in Part B and Part C would ensure a fasten touch between the tungsten wires and the pins in the nine slots.

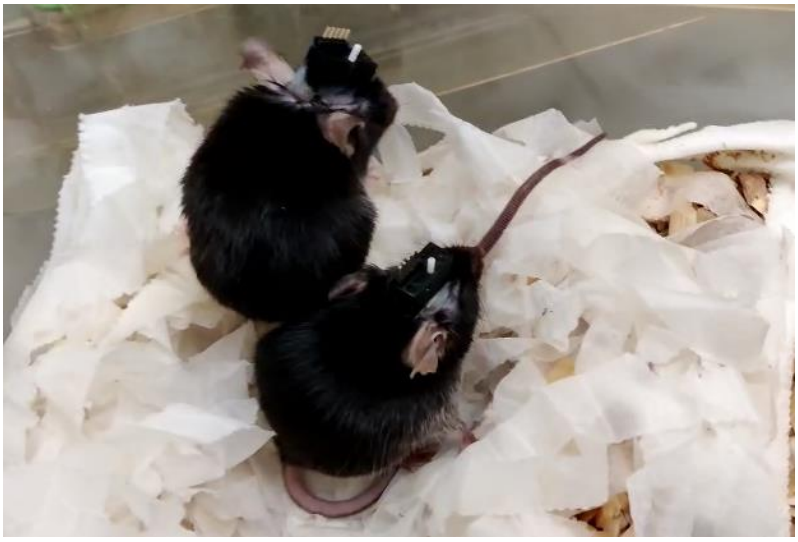

Fig. S4. Two mice with the implanted axialtrode on their heads.

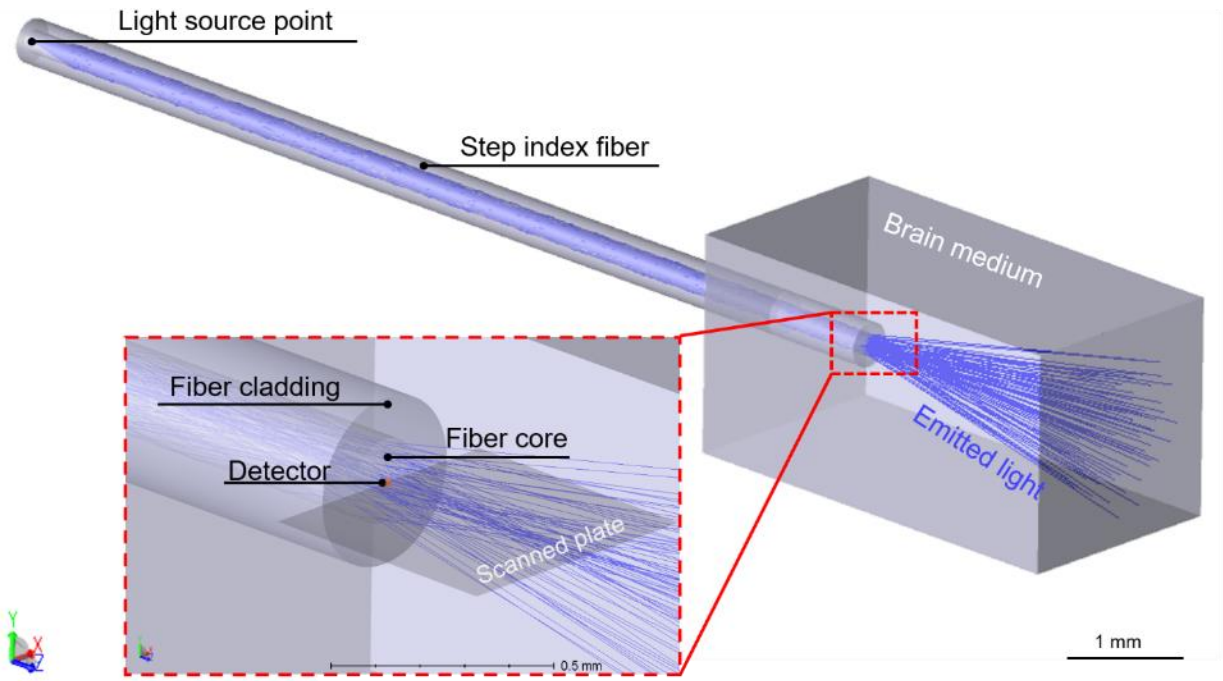

Fig. S5. The model in ray-tracing software Zemax OpticStudio for measuring the illumination map of the optical fibers in the medium of the brain.

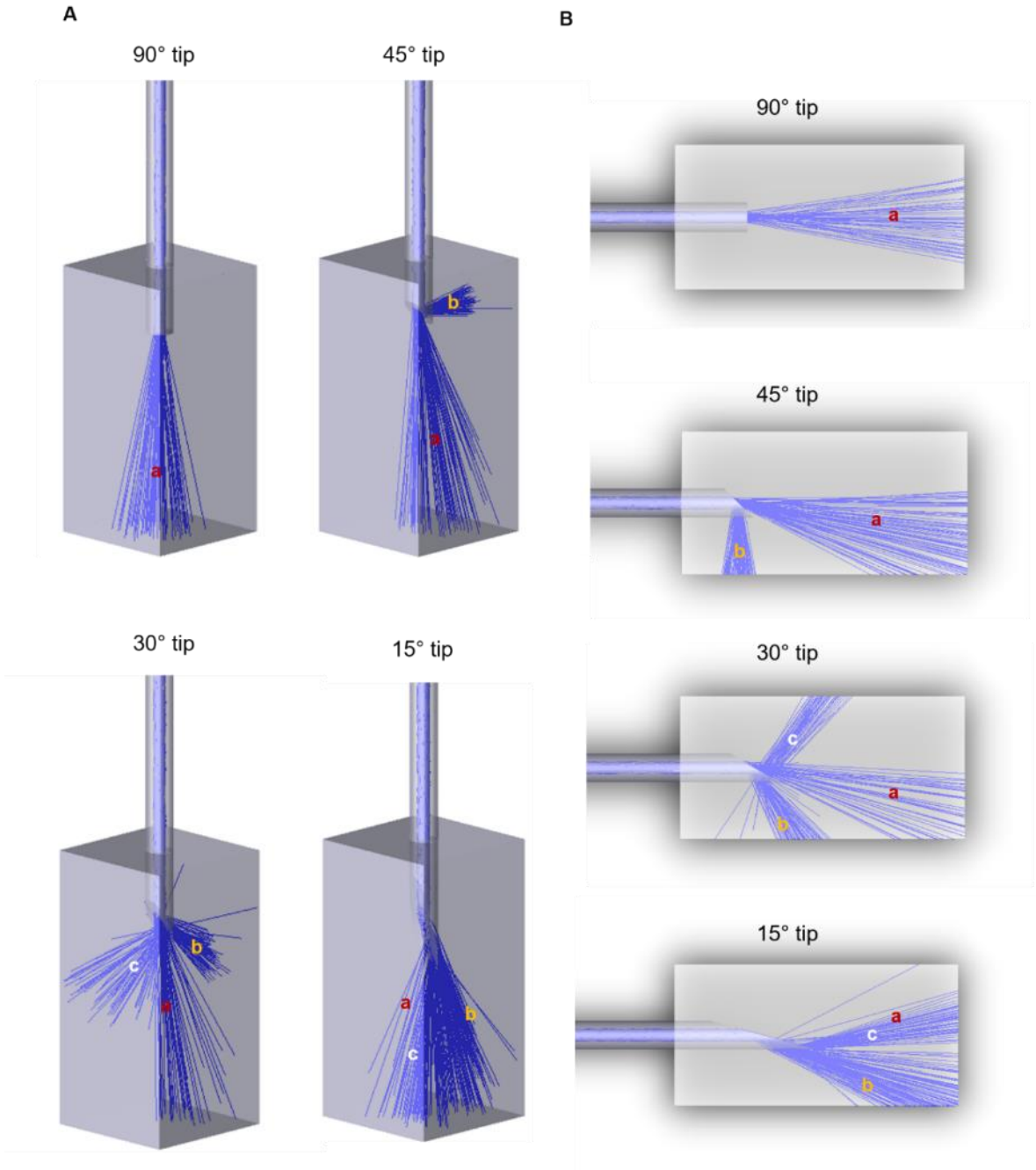

Fig. S6. The (A) 3D model and (B) side view in ray-tracing software Zemax OpticStudio to illustrate the light emission angle variation with the decreasing of the optical fiber tip angle from 90° to 15°. When the tip of the optical fiber is flat (90°), all the rays are emitted to the direction along the length of the fiber (*cluster a*). When a smaller angle is introduced to the tip of the fiber (45°), some of the rays emitted from the fiber end facet are reflected by the interface between the fiber core and brain medium and propagated to the side of the fiber (*cluster b*). As the tip of the fiber becomes shaper (30°), some of the rays in cluster b are reflected by the interface between fiber cladding and the brain medium and propagated to the other side of the fiber (*cluster c*). The angle between *cluster b* and *cluster c* can be reduced with the further decrease of the fiber tip (15°).

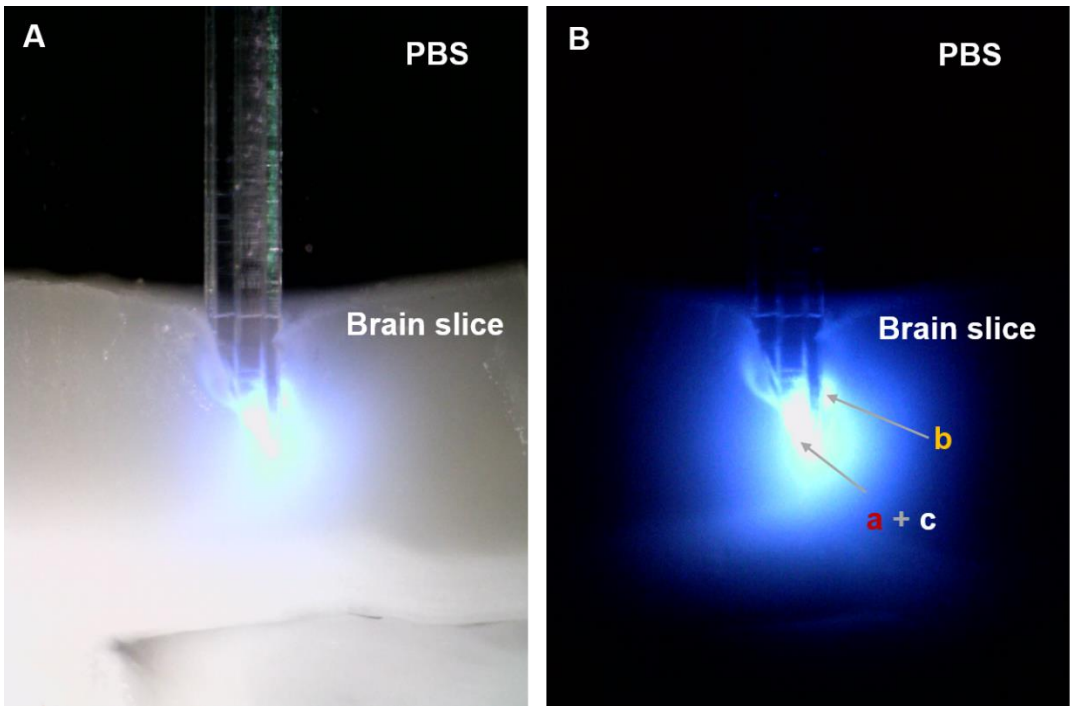

Fig. S7. The illumination map of the angled tip fiber (30°) in brain slices. The tip of the fiber was inserted into the brain slices **(A)** under microscope light for position conformation and **(B)** without microscope light. It can be seen that most of the blue light was emitted from the tip of the fiber, which can match the simulation result from Zemax OpticStudio. However, the illumination map behaved in a strong inhomogeneous because of the randomly squeezed brain tissue during the axialtrode insertion. To reduce these squeezed-tissue-artifacts in the illumination map, a piece of brain slice was cut in the rostral-caudal direction, and the flat upper surface of the cortex was positioned in touch with the end facet of the angled tip fiber as seen in Fig. 2E.

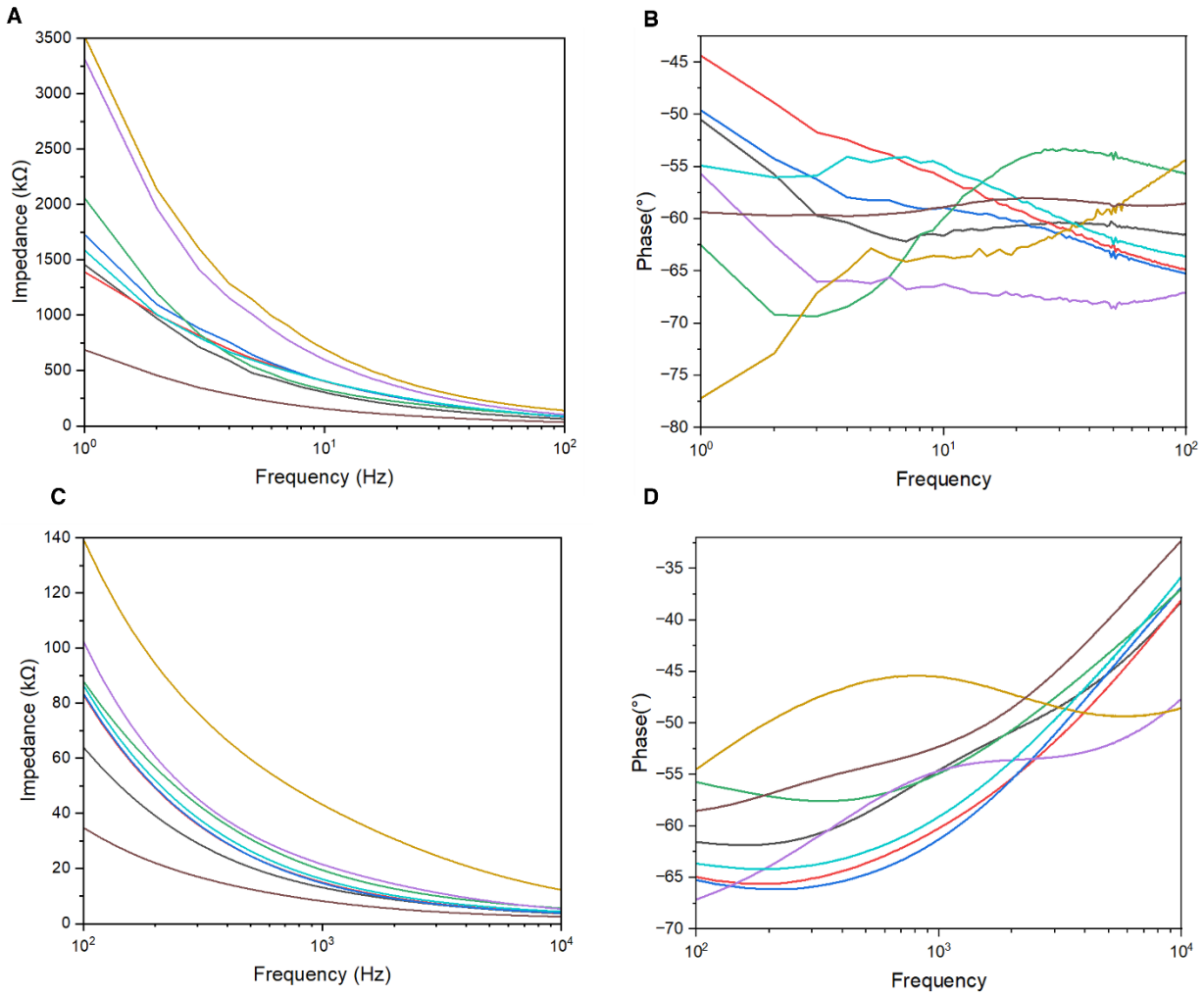

Fig. S8. Impedance spectroscopy of the eight integrated tungsten electrodes of the axialtrode. To enhance visualization, the broadband results are divided into two sub-bands: 1-100 Hz (A and B) and 100-10 kHz (C and D). The measured impedance of all of the eight electrodes integrated into the axialtrode is notably below the threshold for neural activity detection (1 MΩ at 1 kHz). Eight distinct colors are used to represent the measured results from each of the eight electrodes.

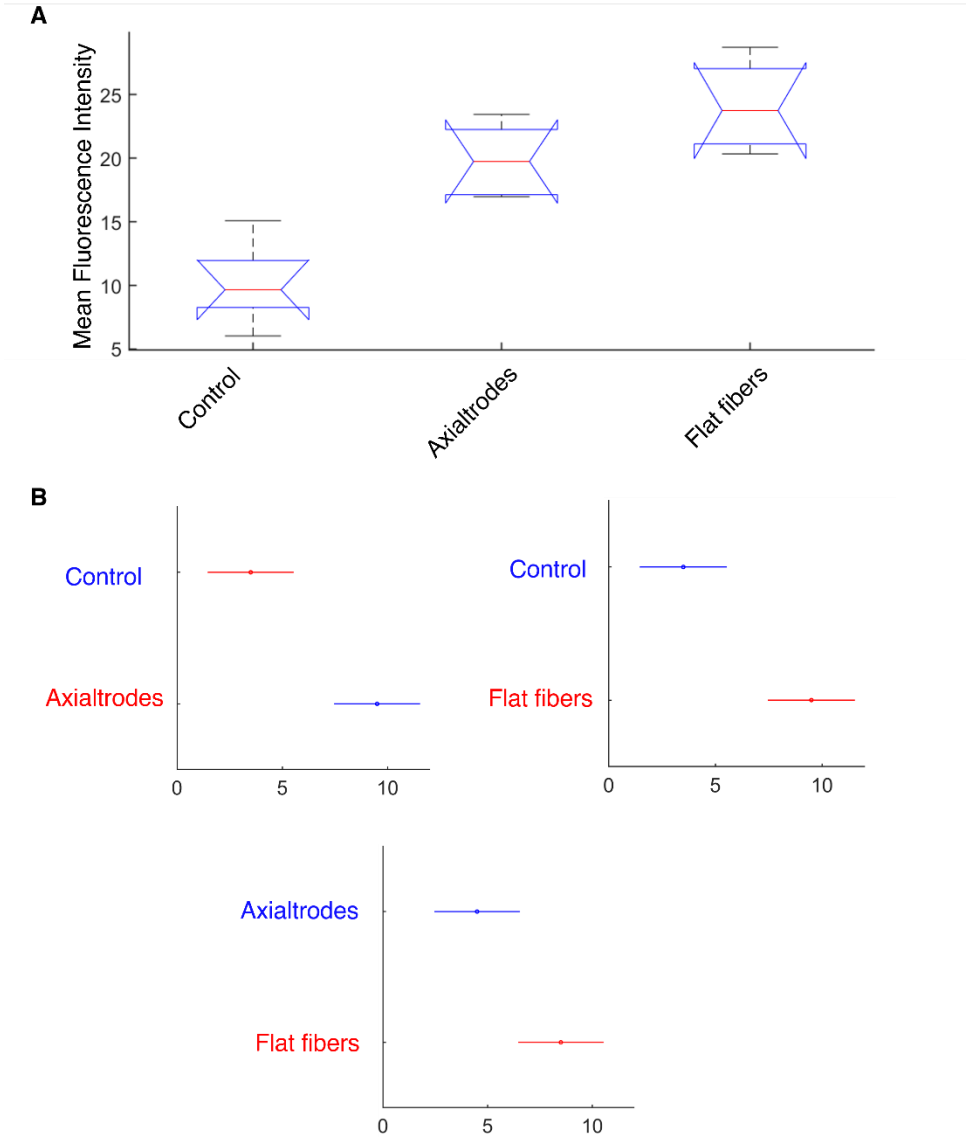

Fig. S9. Statistical significance analysis of the IHC results at the implantation sites. (A) The Kruskal-Wallis test suggests statistically significant ($p<0.05$) differences between the control, axialtrode, and flat fiber groups. **(B)** Pairwise Tukey honest significance tests have been performed for protection against type I errors. The null hypothesis can be rejected at $p<0.05$ by the tests of the Control-flat fiber and control-Axialtrodes pairs. By contrast, the axialtrodes-flat fiber pairs test results in a slightly higher p-value (0.0547).

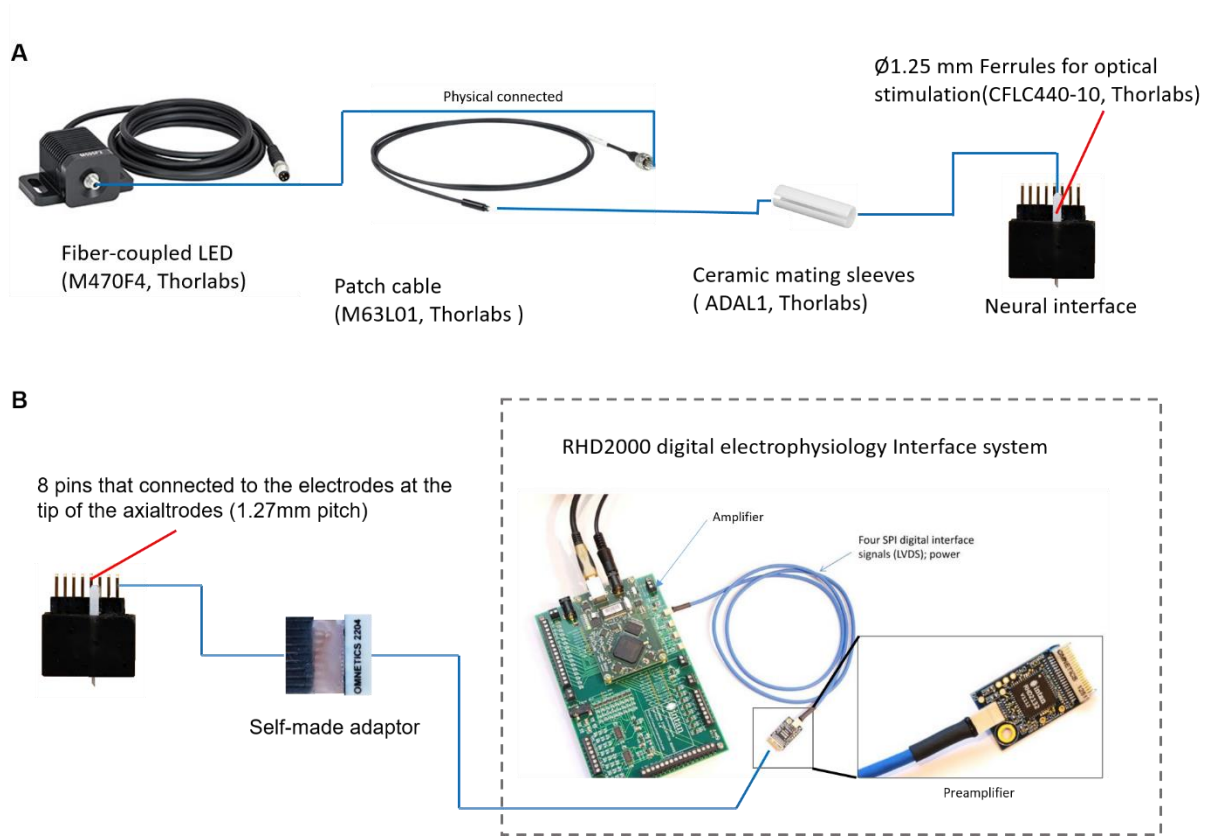

Fig. S10. The schematic of the device's connection for (A) optical stimulation and (B) electrophysiology recordings (The physical connections between the components' ports are represented by blue lines).

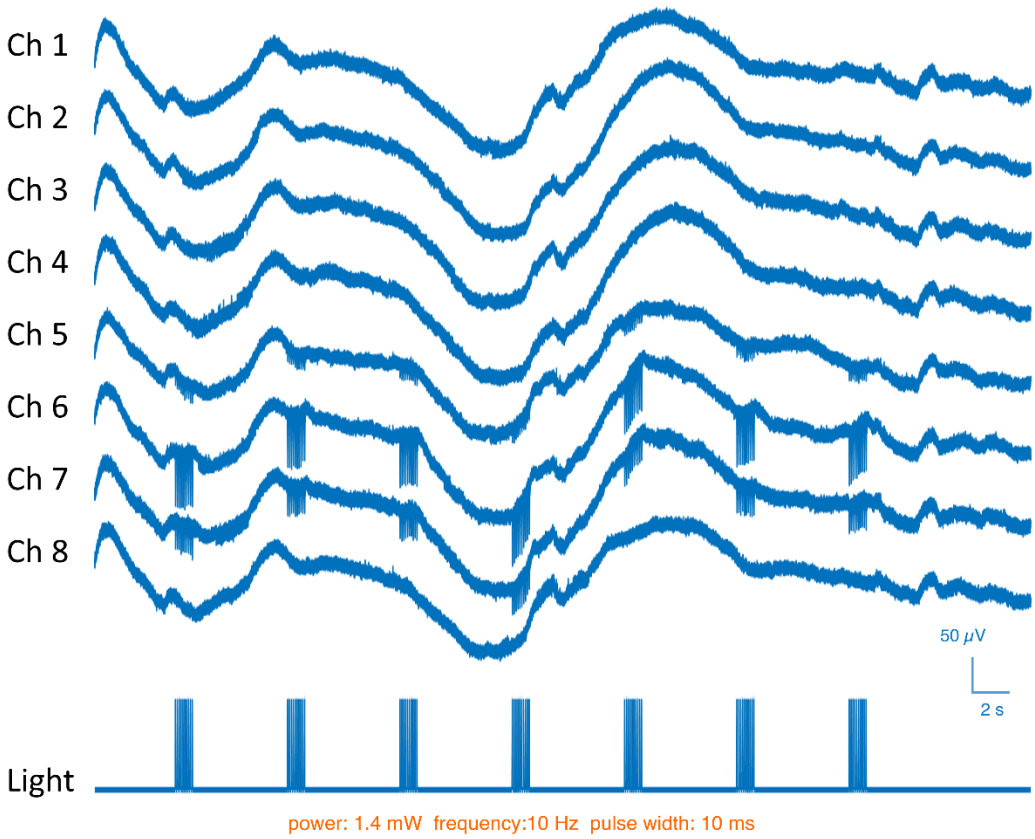

Fig. S11. The full photoelectric artifacts recordings during pulse light stimulation in PBS. The three electrodes near the tip of the axialtrodes (Ch5, Ch6, and Ch7) behave with light-induced electric signals while the light stimulation has a negligible effect on the other electrodes.

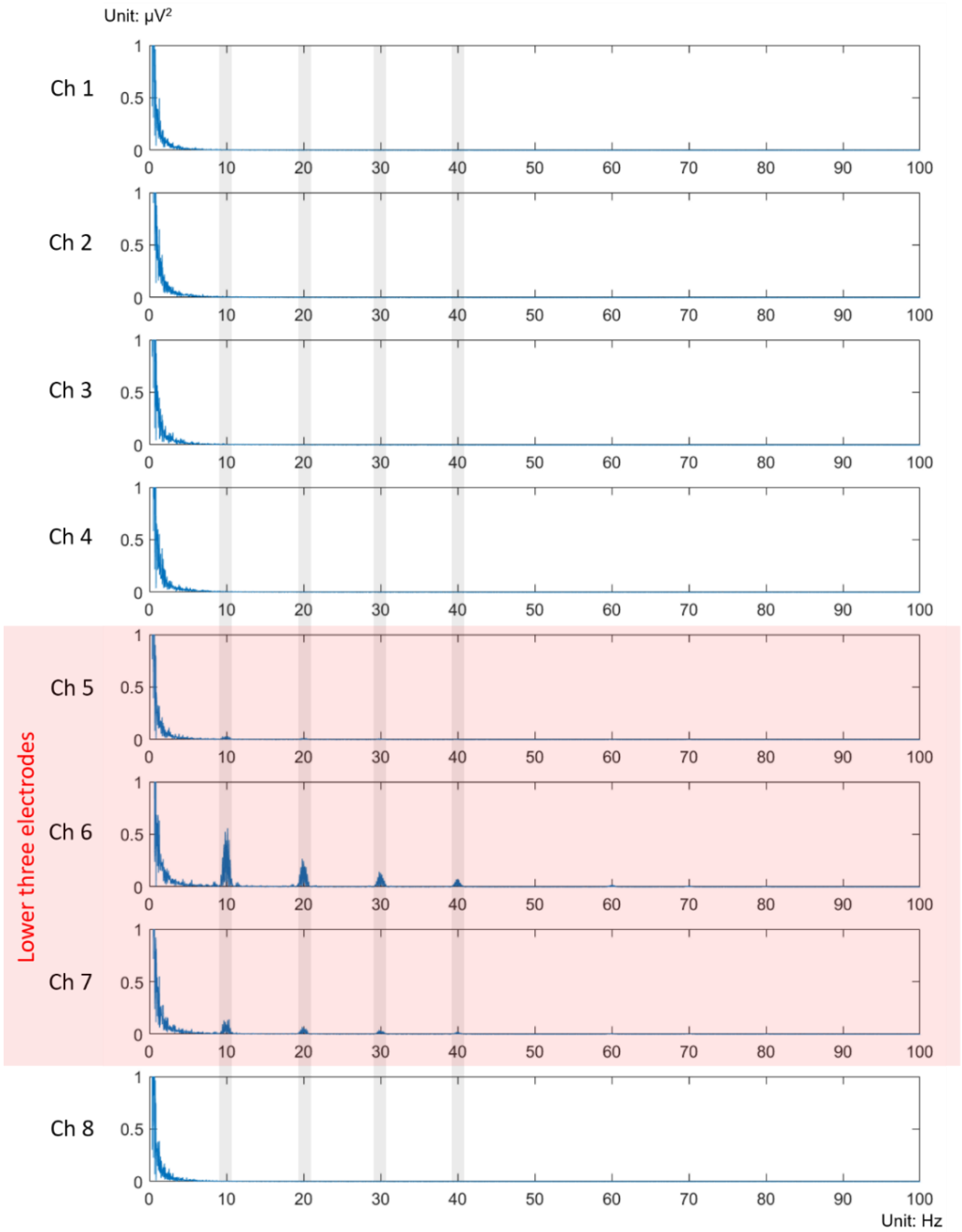

Fig. S12. The power spectrum of the light-evoked artifacts collected by the distributed eight electrodes in the axialtrode. It is clear that the photoelectric artifacts have the same frequency as the stimulation light (10 Hz) and its overtones (20, 30, and 40 Hz). The power of the photoelectric artifacts keeps decreasing at a higher frequency band. This makes it possible to minimize the photoelectric artifacts by using a high-pass filter. In addition, the light-evoked artifacts are mainly observed in the lower three electrodes in the neural interface. This is due to that most of the light propagating in the fiber core would emitted from the tip of the fiber when a small tip angled is introduced to the axialtrodes, as illustrated in **fig. S6**. Therefore, only the lower three electrodes have been illuminated by the stimulation light in the PBS medium.

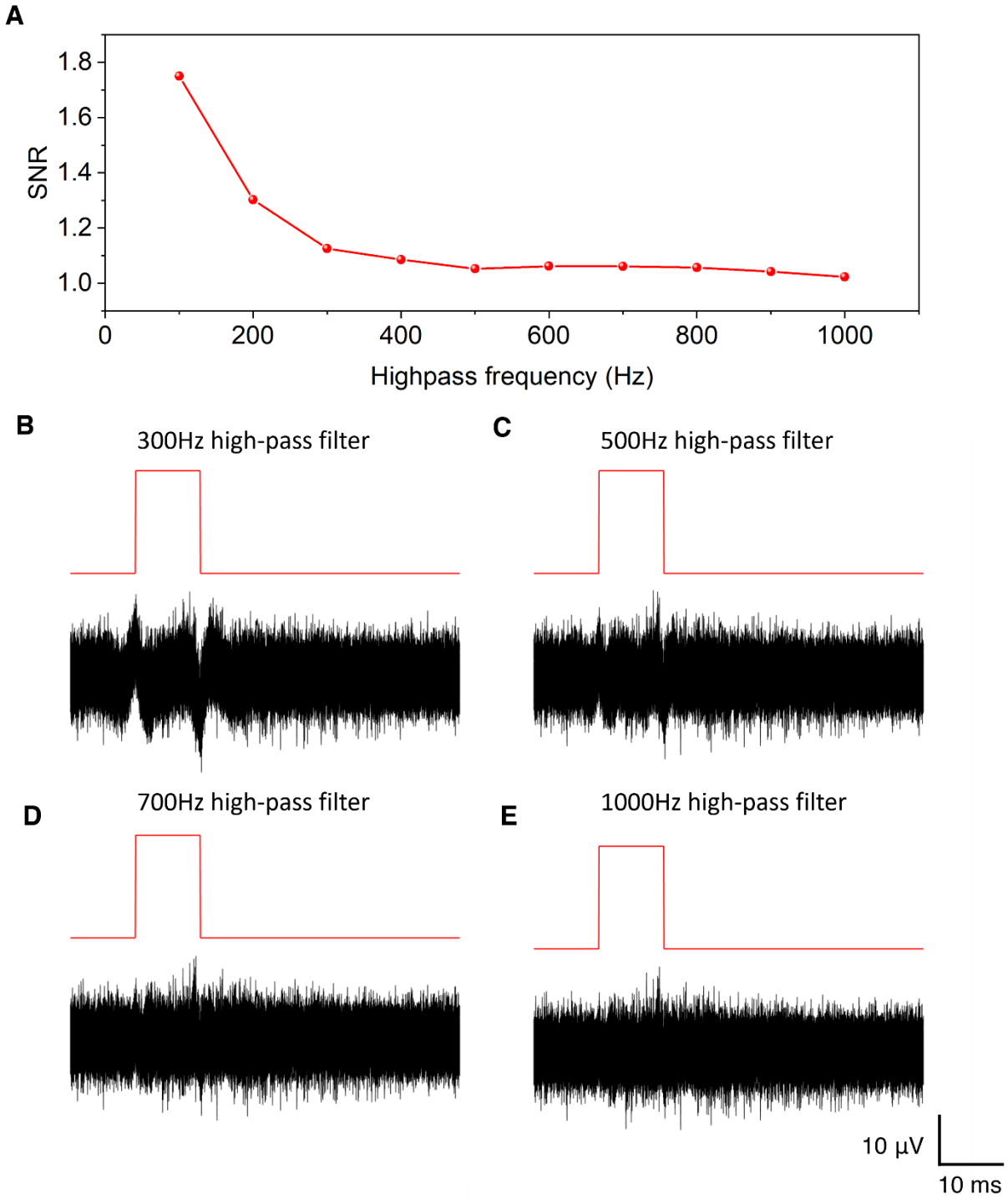

Fig. S13. The highpass filter analysis to minimize the photoelectric artifacts. (A) Different highpass filters are applied to the recorded data from Ch6 (which exhibits the strongest photoelectric artifacts) in fig. S11 to calculate the photoelectric artifacts SNR under light stimulation. It can be seen that there are some residential photoelectric artifacts after using a 300 Hz highpass filter (B), while the artifacts can be minimized when increasing the frequency of the highpass filter to 500 Hz (C), (D), and (E).

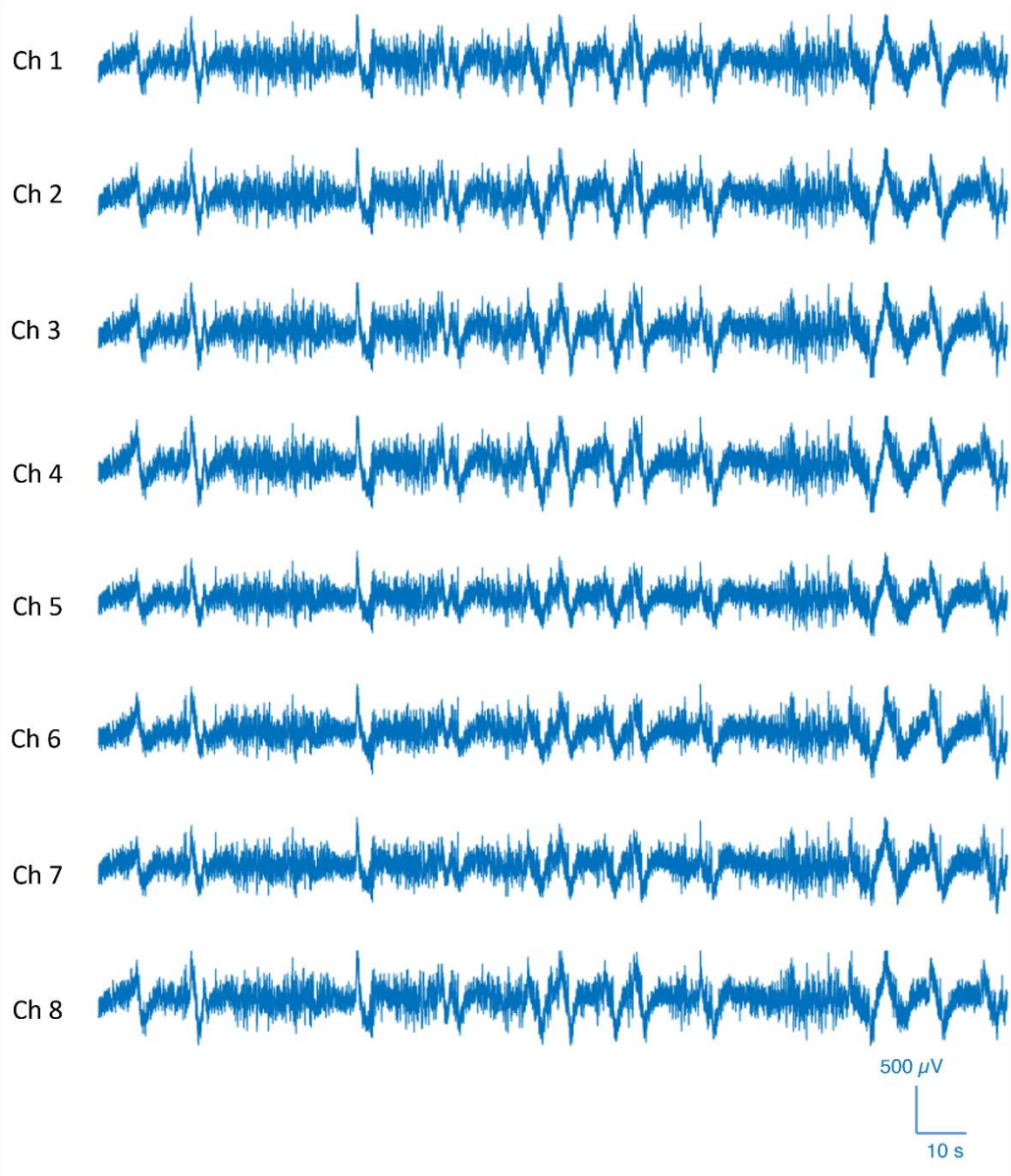

Fig. S14. Full electrophysiology recordings by the axialtrodes. Ch1 to Ch8 correspond to the eight electrodes integrated into the axialtrodes.

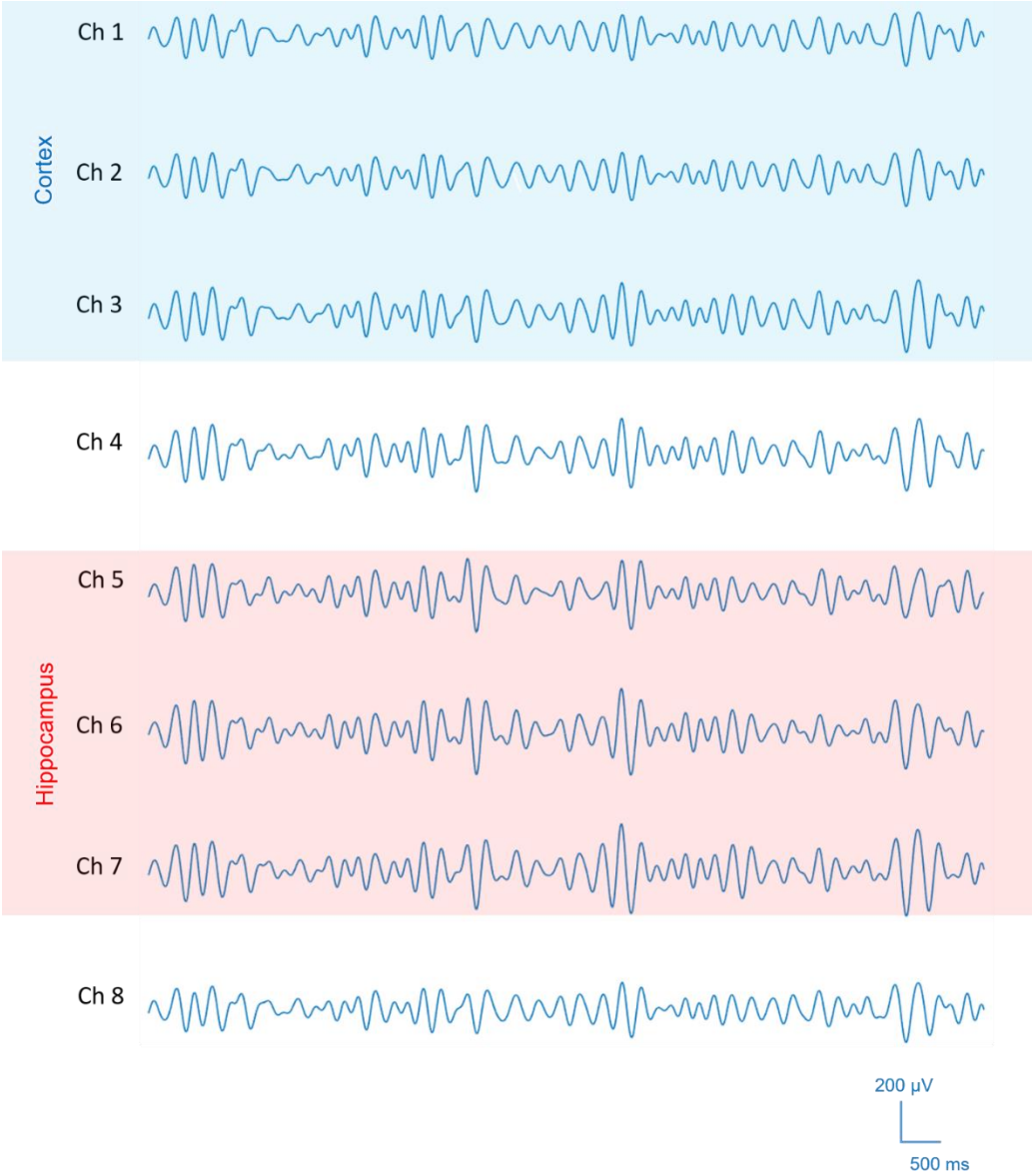

Fig. S15. The theta rhythm component of the electrophysiology recordings by the axialtrode. The signals from Ch1, Ch2, and Ch3 correspond to the recording from the upper three electrodes positioned at the cortex (blue shadow) while the signals from Ch5, Ch6, and Ch7 correspond to the recording from the lower three electrodes that are aligned to the hippocampus (red shadow) of the mouse brain.

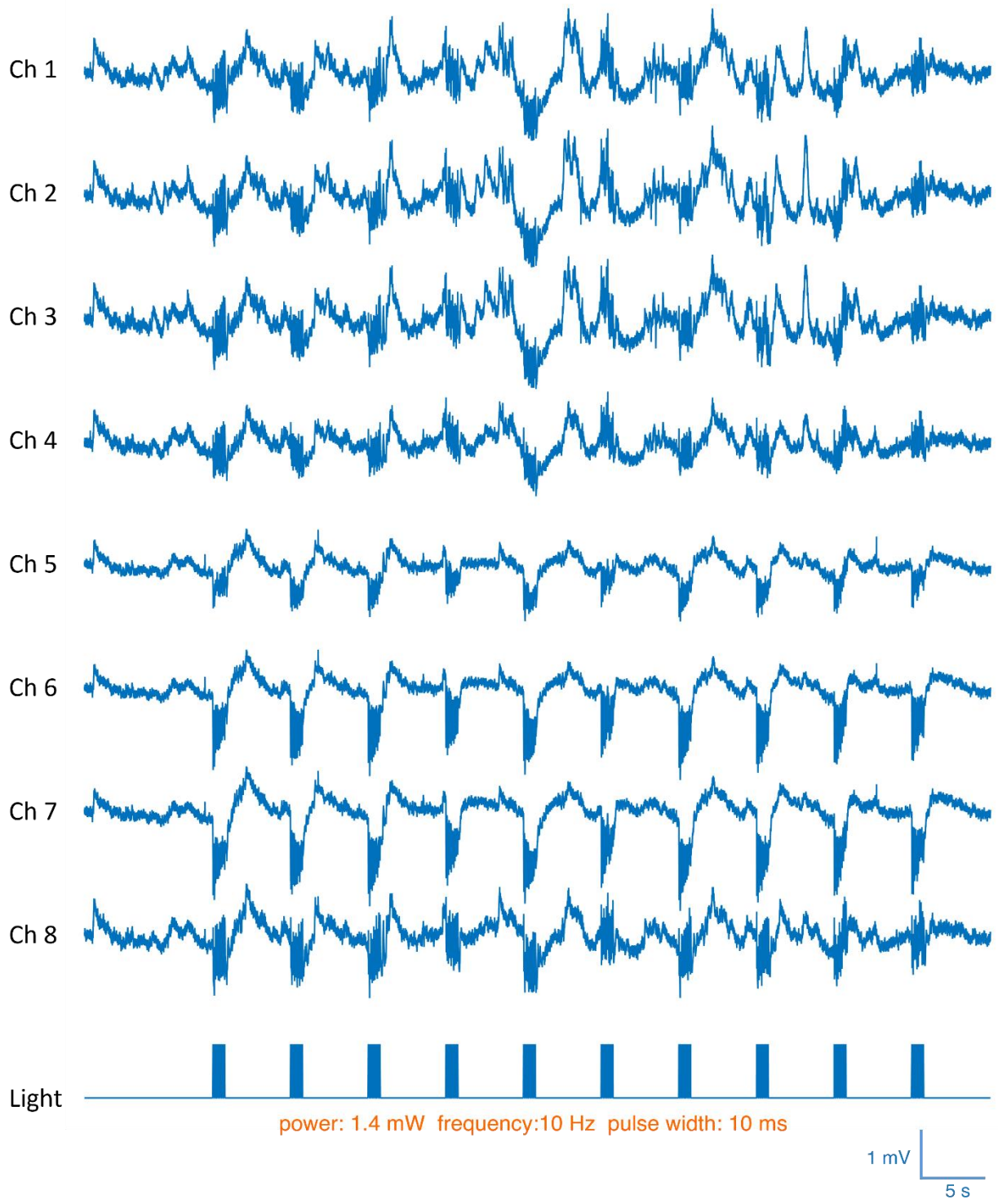

Fig. S16. Typical electrophysiological recordings using the axialtrode in optogenetic experiments demonstrate brain extracellular responses to light-induced activity. This activity is elicited by 10 millisecond light pulses delivered at a frequency of 10 Hz and is collected by the eight integrated electrodes of the axialtrode.

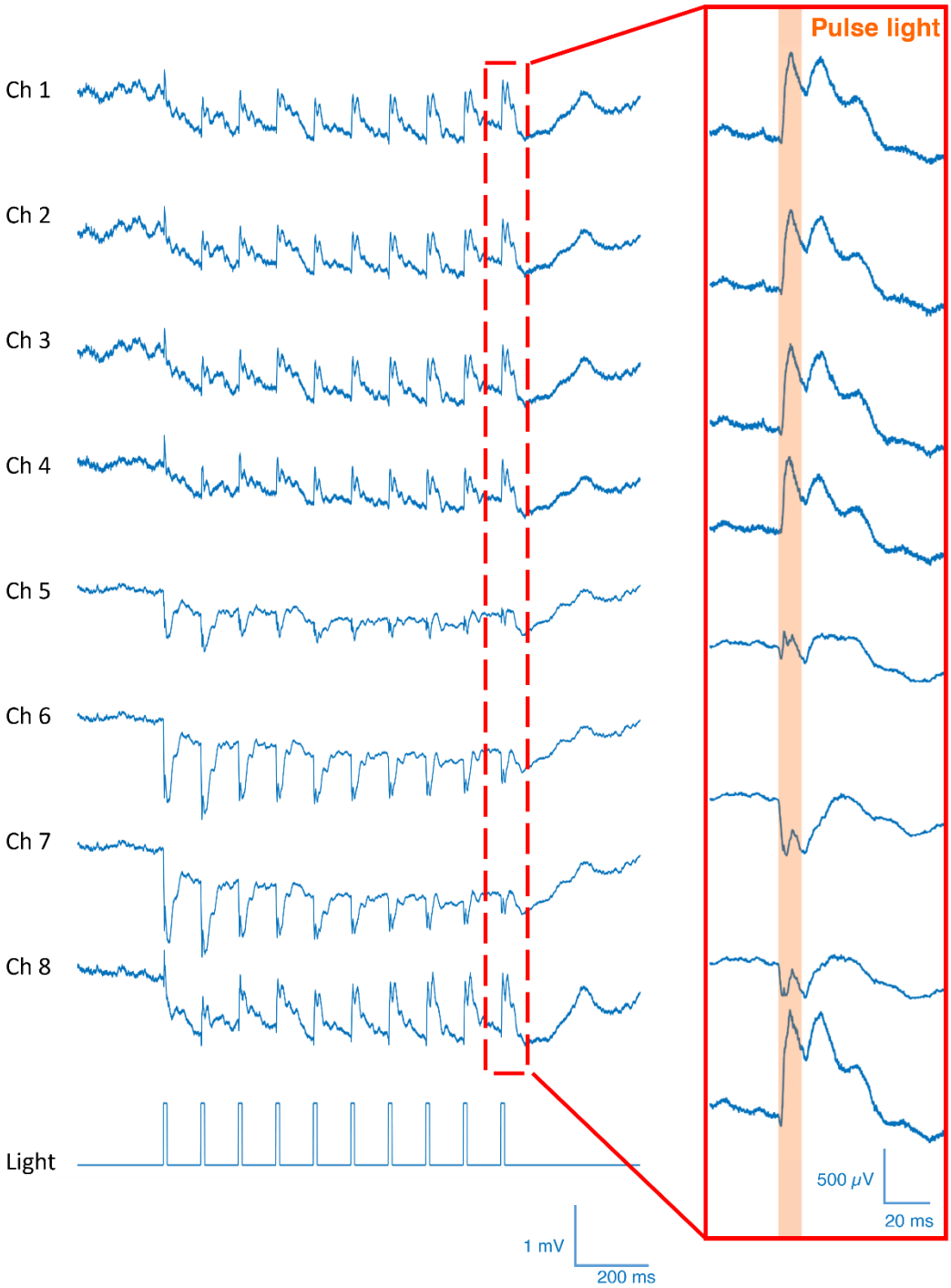

Fig. S17. Typical 1s electrophysiological recordings using the axialtrode in optogenetic experiments to show the details of the eight traces in fig. S16.

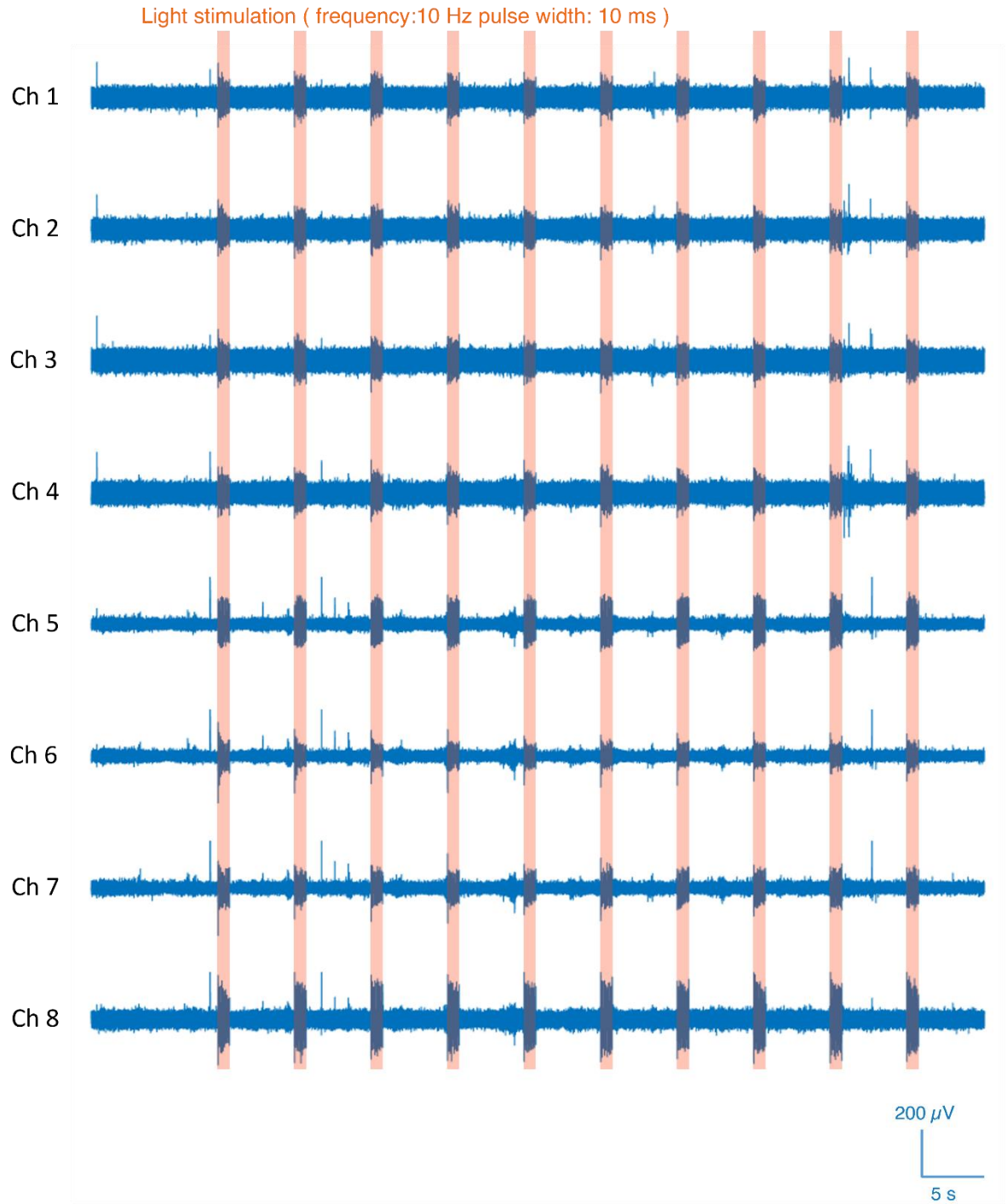

Fig. S18: Optogenetic control of action potential firing in mouse brain. For the recordings presented in fig. S14, a high-pass filter (>500 Hz) was used to highlight the recorded neural activities.
interface

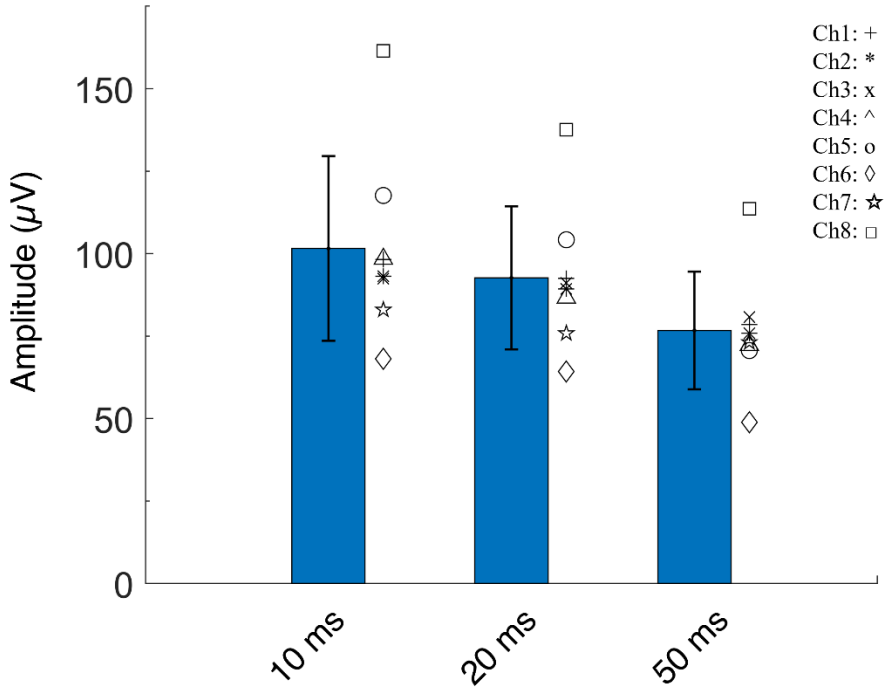

Fig. S19. The evoked neural activity amplitude from all eight electrodes during optical stimulation with different pulse widths (10 ms, 20 ms, and 50 ms).

Table S1 The SNR of the spikes under different light pulse stimulation

Pulse width (ms)	Spikes amplitude (μV)	Noise amplitude (μV)	SNR
10	101.55	37.26	2.93
20	92.67	37.81	2.61
50	76.71	38.98	2.01

Movie S1.

The mice with the implanted axialtrode.

Movie S2.

The schematic of the neural activity recording process with the proposed axialtrode.

.